AGU ADVANCING EARTH AND SPACE SCIENCE

Earth and Space Science

Key Points:

- Significant near trench slip on the plate interface of the 2021 Loyalty Islands earthquake was estimated by inverting coastal and offshore tsunami waveforms
- Accurate tsunami forecast can be obtained from interpolating results of precomputed earthquake scenarios
- The new New Zealand DART network is essential in improving the tsunami warning capability for countries in the South West Pacific

Supporting Information:

Supporting Information may be found in the online version of this article.

Correspondence to:

A. R. Gusman,
a.gusman@gns.cri.nz

Author Contributions:

Conceptualization: Aditya Riadi Gusman, Jean Roger, William Power
Data curation: Aditya Riadi Gusman, Jean Roger, Yoshihiro Kaneko
Formal analysis: Aditya Riadi Gusman, Jean Roger, William Power, Bill Fry, Yoshihiro Kaneko
Funding acquisition: Bill Fry

The 2021 Loyalty Islands Earthquake (Mw 7.7): Tsunami Waveform Inversion and Implications for Tsunami Forecasting for New Zealand

Aditya Riadi Gusman[1] , **Jean Roger[1]** , **William Power[1]**, **Bill Fry[1]**, and **Yoshihiro Kaneko[2]**

[1]Earth Structures and Processes, GNS Science, Lower Hutt, New Zealand, [2]Department of Geophysics, Graduate School of Science, Kyoto University, Kyoto, Japan

Abstract A tsunamigenic earthquake with thrust faulting mechanism occurred southeast of the Loyalty Islands, New Caledonia, in the Southern Vanuatu subduction zone on the 10th of February 2021. The tsunami was observed at coastal gauges in the surrounding islands and in New Zealand. The tsunami was also recorded at a new DART network designed to enhance the tsunami forecasting capability of the Southwestern Pacific. We used the tsunami waveforms in an inversion to estimate the fault slip distribution. The estimated major slip region is located near the trench with maximum slip of 4 m. This source model with an assumed rupture velocity of 1.0 km/s can reproduce the observed seismic waves. We evaluated two tsunami forecasting approaches for coastal regions in New Zealand: selecting a pre-computed scenario, and interpolating between two pre-computed scenarios. For the evaluation, we made a reference map of tsunami threat levels in New Zealand using the estimated source model. The results show that the threat level maps from the pre-computed Mw 7.7 scenario located closest to the epicenter, and from an interpolation of two scenarios, match the reference threat levels in most coastal regions. Further improvements to enhance the system toward more robust warnings include expansion of scenario database and incorporation of tsunami observation around tsunami source regions. We also report on utilization of the coastal gauge and DART station data for updating forecasts in real-time during the event and discuss the differences between the rapid-response forecast and post-event retrospective forecasts.

Plain Language Summary We estimated the tsunami source of the 2021 Loyalty Islands earthquake from inversion of tsunami waveforms recorded at offshore DART and coastal stations. These DART stations are part of a new DART network that was designed to enhance the tsunami forecasting capability of New Zealand and the Southwestern Pacific region. The inversion result suggest that the earthquake ruptured the plate interface with relatively large slip near the trench. Our source model can well reproduce the observed tsunami and seismic waveforms. The tsunami threat level map for New Zealand coastal regions produced from the source model is then used as a reference map to evaluate two techniques for rapid tsunami forecasting. Both techniques utilize pre-computed earthquake scenarios. The first technique is using the epicenter and magnitude of the earthquake to select the nearest earthquake scenario. The second technique interpolates pre-computed results of two earthquake scenarios around the epicenter. The tsunami hindcast accuracies from the two techniques are high as the resulting tsunami threat levels matched the reference ones at most of the warning regions. Potential improvements to enhance the system toward more robust warnings include expansion of the scenario database and incorporation of tsunami observations around the source regions.

1. Introduction

One of subduction zones in the Pacific Ocean that poses tsunami threats to New Zealand and other southwest Pacific states is the Vanuatu (also known as New Hebrides) subduction zone. In this region, thrust earthquakes occur on the plate interface between the subducting Australia plate and the overriding Vanuatu arc and North Fiji Basin (Calmant et al., 2003). On the 10th of February 2021, a magnitude (Mw) 7.7 earthquake occurred in this subduction zone and generated a tsunami (Figure 1). Based on the earthquake's magnitude, location and depth, a tsunami warning was issued by the Pacific Tsunami Warning Center (PTWC) for island nations around the epicenter in the Southwest Pacific such as New Caledonia, Fiji, Vanuatu, Tonga, New Zealand, and Australia. The National Emergency Management Agency (NEMA) of New Zealand issued tsunami threat warnings for several coastal regions in the country.

Investigation: Aditya Riadi Gusman, Jean Roger, Yoshihiro Kaneko
Methodology: Aditya Riadi Gusman, Jean Roger, Yoshihiro Kaneko
Software: Aditya Riadi Gusman
Validation: Aditya Riadi Gusman, Jean Roger, William Power, Yoshihiro Kaneko
Visualization: Aditya Riadi Gusman, Jean Roger, Yoshihiro Kaneko
Writing – original draft: Aditya Riadi Gusman, Jean Roger, William Power, Bill Fry, Yoshihiro Kaneko
Writing – review & editing: Aditya Riadi Gusman, Jean Roger, William Power, Bill Fry, Yoshihiro Kaneko

According to the United States Geological Survey (USGS), the earthquake occurred at 13:19:55 UTC with a hypocenter located at 23.051°S–171.657°E and 10 km depth southeastward of the Loyalty Islands archipelago, New Caledonia, and south of Aneityum, Vanuatu, in the southern part of the Vanuatu subduction zone. It is located to the east of the region where the Loyalty Ridge, part of the Australian Plate, is subducted under the overriding Pacific Plate at a convergence rate of ∼12 cm/yr and where Mw7.0+ tsunamigenic earthquakes occurred during the last century (Roger et al., 2021). Since the 17 May 1995 Mw 7.7 Walpole tsunamigenic earthquake, the Vanuatu subduction zone, which is amongst the most seismically active, has produced at least 12 small (amplitude < 50 cm) to moderate (0.5 m < amplitude < 5 m) tsunamis. These tsunamis were triggered by earthquakes, such as the 19 November 2017 Mw 7.0 earthquake or the 5 December 2018 Mw 7.5 Tadine earthquake (Figure 1) whose maximum amplitude reached more than 2 m in New Caledonia and 4 m in Aneityum Island, Vanuatu (Roger et al., 2019, 2021; Sahal et al., 2010). Although the central and northern part of the Vanuatu subduction zone is also known to have experienced tsunamis triggered by even larger earthquakes of Mw 8.0+ (Ioualalen et al., 2017), there is no clear evidence for Mw8.0+ earthquakes in the southeasternmost part of the subduction zone (170°E−175°E), where the 10 February 2021 earthquake occurred. Lack of recorded large events may also have a physical explanation. In this region, the megathrust is no longer eastward dipping, as is the case for the rest of the subduction zone, but instead oriented N17°E perpendicular to the trench with a rate measured at ∼5 cm/yr, making it the slowest converging part of the Vanuatu convergence zone (Calmant et al., 2003).

The focal mechanisms provided by the Global Centroid Moment Tensor (GCMT) and USGS W-phase Moment Tensor (WMT) solutions suggest that the earthquake resulted of a rupture of the plate interface showing a nearly pure thrusting mechanism. The GCMT solution gives a seismic moment (M_o) of 4.01×10^{20} Nm and nodal planes with strike = 279°/87°, dip = 23°/67°, and rake = 101°/85°. The USGS WMT solution gives a seismic moment of 4.36×10^{20} Nm and nodal planes with strike = 246°/92°, dip = 17°/75°, and rake = 65°/97°. The USGS finite fault model for the thrust faulting event maps earthquake rupture all the way to the trench with moment rate maximum at 15 s after earthquake origin time and rupture termination within 40 s.

This geometry of nearly pure thrusting earthquakes can trigger tsunamis with a main energy axis orientation of South-Southwest/North-Northeast, that is, toward New Zealand and Southeastern Australia to the south and toward Vanuatu to the north (Okal, 1988). Thus, the tsunami from the 2021 Loyalty Islands earthquake propagated in the southwestern region of the Pacific Ocean, and was recorded at local coastal gauges in New Caledonia and Vanuatu, and also at regional distances in places like Fiji, Western Samoa, Tuvalu, Australia (including Tasmania) and New Zealand, more than 3000 km away from the earthquake epicenter (Figures 1 and 2 and Table 1). The tsunami was also recorded by the New Zealand network of DART stations in the Hikurangi-Kermadec-Tonga subduction zone (Figure 2) (Fry et al., 2020). Deployment of this network was started by the government of New Zealand in December 2019 (DART NZA, B, C, E, and F), September 2020 (DART NZG, H, and I) and July 2021 (DART NZD, J, K, and L). It was designed to enhance the capability of New Zealand and other Pacific states to detect and forecast tsunamis in the Southwestern Pacific and was strongly motivated by the recognized gap in operational response to events occurring at regional propagation distances (Fry et al., 2018; Power et al., 2018).

The procedures for tsunami early warning in New Zealand make use of a two-stage approach involving initial issuance of "action maps" and subsequent "threat maps". The action maps are based on highly uncertain early magnitude estimates. They are designed to rapidly and conservatively assess the possibility of land threat and trigger activation of emergency response. They are binary maps, assigning "land threat" or "under assessment" to coastal zones. This early forecast is based on pre-computed tsunami scenarios and simple 1D tsunami prediction equations (Power, 2017). Following refinement of earthquake source parameters, typically derived through available W-phase moment tensor inversions, precomputed tsunami scenarios from earthquake sources located in subduction zones around the Pacific Ocean are used to issue threat level maps. Tsunami threat level maps contain the forecasted tsunami heights within New Zealand's coastal regions (tsunami warning regions). The precomputed tsunami scenario catalog contains a total of ∼1,000 uniform fault slip models with earthquake magnitudes ranging from 6.9 to 9.3 (Gusman, Lukovic, & Peng, 2020). A tsunami threat level map for coastal regions in New Zealand was prepared for every earthquake scenario. Pre-computed tsunami waveforms at coastal gauges and DART stations are available too. In this database, there is a scenario available with the same magnitude and a location very close to the 2021 Loyalty Islands earthquake.

Facing the enduring threat of tsunamis affecting their coastal populations and infrastructures, many countries have built tsunami pre-computed scenarios databases to support tsunami preparation and response, for example,
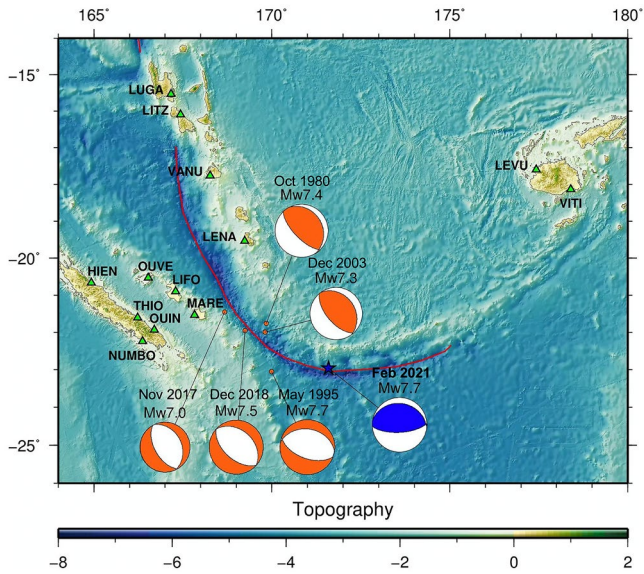
Figure 1. Major tsunamigenic earthquakes in the Vanuatu subduction zone from 1980. Focal mechanisms are based on GCMT solutions. Green triangles indicate coastal gauges at which the tsunami waveforms used in this study were recorded. Convergent plate boundaries are indicated by red lines.
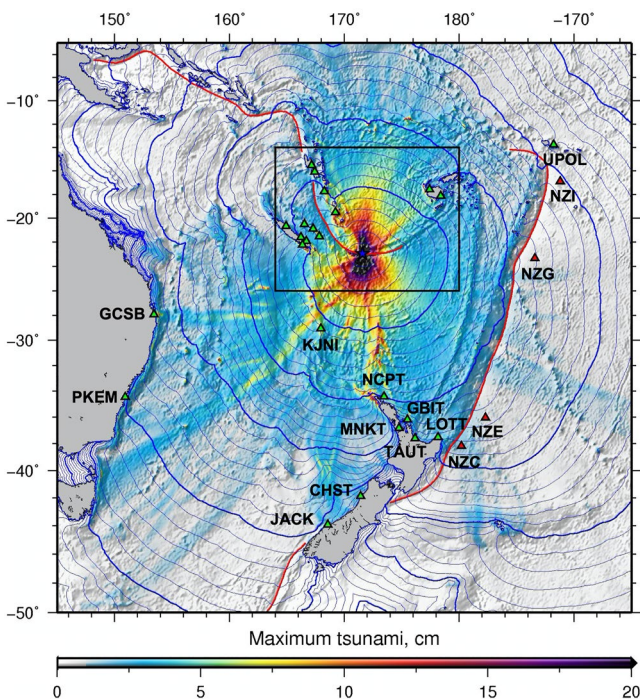

Figure 2. Maximum tsunami amplitude distribution from the 2021 Loyalty Islands earthquake source model and theoretical travel time from the epicenter calculated using bathymetry data. Thick blue contour lines indicate time intervals of 1 hr, while thin blue contour lines indicate time intervals of 10 min. Green and red triangles indicate coastal gauges and DART stations, respectively, at which the tsunami waveforms used in this study were recorded. Plate boundaries are indicated by red lines. Stations names for the green triangles inside the black rectangle can be seen in Figure 1.

Japan (Hoshiba & Ozaki, 2014; Tatehata, 1997), French Polynesia (Reymond et al., 2012), Turkey (Onat & Yalciner, 2013), Australia (Greenslade et al., 2011), Indonesia (Harig et al., 2019), Portugal (Matias et al., 2012), and New Caledonia (Duphil et al., 2021). High resolution tsunami inundation forecasting through scenario selection of pre-computed scenarios, or deep learning using pre-computed scenarios, have also been considered (Gusman et al., 2014; Mulia et al., 2018, 2020). Ways to improve the use of those databases, and the accuracy of impact forecasting, especially for scenarios whose magnitude or location lie outside the ranges of the existing ones, are of major interest.

In this paper, the tsunami waveforms recorded at coastal gauges and DART stations are used in an inversion process to estimate the non-uniform fault slip distribution of the earthquake. We then assess the fault slip model using simulations of seismic wave propagation and seismic waveform data. Next, a custom tsunami threat level map in New Zealand made from the earthquake source model was used as a reference map (ground truth) to evaluate our tsunami forecasting approach. We compare the reference threat level map with the map for the nearest Mw 7.7 scenario to the epicenter. We also evaluate a map created by interpolating the result from two Mw 7.7 scenarios around the epicenter. Here we describe the interpolation method to produce an interpolated threat level map and tsunami waveforms at observation points. Finally, we discuss the effectiveness of the pre-computed scenarios for providing accurate tsunami forecasts for New Zealand coastal regions. We conclude by describing response forecast calibration based on data from coastal tide gauges and DART stations.

2. Tsunami Waveform and Bathymetric Data

2.1. Tsunami Waveforms

The tsunami generated by the 2021 Loyalty Islands earthquake was clearly recorded at coastal gauges in New Caledonia, Vanuatu, Fiji, Australia, Samoa, and New Zealand. The coastal gauge records were available from the IOC water level monitoring website (http://www.ioc-sealevelmonitoring.org, last accessed on 23 May 2022). We first approximated the tides by fitting a 7th degree polynomial to the original record and then removed them from the original record to obtain the tsunami waveforms. The details for the polynomial fitting method can be found in Heidarzadeh et al. (2015). The tsunami was also recorded at DART stations NZC, NZE, NZG, and NZI which are located eastward of the Hikurangi-Kermadec-Tonga subduction zone trench (Figure 2). We also removed the tides recorded at the DARTs by the polynomial fitting method. Then high frequency waves were removed using a 4th-order low pass Butterworth filter with cutoff period of 200 s to get the tsunami waveforms. Table 1 shows the observed maximum tsunami amplitudes and travel times at the coastal gauges and DART stations.

2.2. Bathymetric Data and Modeling Grids

A nested grid configuration can be implemented in tsunami simulations to balance computational efficiency and numerical accuracy. There are two nested grid configurations used in this study. One is to simulate the synthetic waveforms for the inversion Green's functions, and the other one is used to calculate the tsunami threat levels in New Zealand.

Table 1
Coastal Gauge and DART Station Information and the Tsunami Record Summaries Sorted by the Station Distance From Epicenter

Station code	Location	Country/region	Longitude	Latitude	Distance from epicenter (km)	First wave amplitude (cm)	Travel time (minute)	Maximum amplitude (cm)
MARE	Maré	New Caledonia	167.8333	−21.5333	418	6.5	49	17.8
LENA	Lenakel	Vanuatu	169.2333	−19.5333	452	12.8	60	135.1
LIFO	Lifou	France	167.3000	−20.9000	498	16.6	68	36.6
OUIN	Ouinné	New Caledonia	166.7000	−21.9333	515	16.5	72	27.2
NUMBO	Nouméa	New Caledonia	166.3667	−22.2333	542	1.7	107.5	4.2
THIO	Thio	New Caledonia	166.2333	−21.6000	571	8.1	80	9.8
OUVE	Ouvéa	New Caledonia	166.5333	−20.5333	587	6.8	103	12.7
VANU	Port Vila	Vanuatu	168.2667	−17.7667	673	6.2	122	5.2
HIEN	Hienghène	New Caledonia	164.9333	−20.6667	732	4.1	101	9.5
KJNI	Norfolk Island	Australia	167.9667	−29.0667	769	11.4	88	43.6
LEVU	Lautoka	Fiji	177.4333	−17.6000	852	3.0	123	5.6
LITZ	Litzlitz	Vanuatu	167.4333	−16.1000	878	2.4	115	8.0
VITI	Suva	Fiji	178.4000	−18.1333	888	4.8	97	4.8
LUGA	Luganville	Vanuatu	167.1667	−15.5333	947	4.1	137	8.6
NCPT	North Cape	New Zealand	173.4667	−34.4333	1,288	3.4	131	28.8
GBIT	Great Barrier Island	New Zealand	175.5000	−36.2000	1,519	8.8	164	62.8
AUCT	Auckland	New Zealand	174.7667	−36.8333	1,571	3.1	250	8.3
TAUT	Tauranga	New Zealand	176.1667	−37.6000	1,684	1.3	189	3.9
LOTT	East Cape	New Zealand	178.1667	−37.5333	1,737	6.2	164	23.9
GCSB	Gold Coast	Australia	153.4333	−27.9333	1,902	20.5	240	30.5
UPOL	Apia	Samoa	188.2333	−13.8000	2,026	1.4	223	4.2
CHST	Charleston	New Zealand	171.4333	−41.9000	2,105	Not observable	Not observable	31.5
JACK	Jackson Bay	New Zealand	168.5667	−43.9667	2,351	12.8	315	35.5
PKEM	Port Kembla	Australia	150.9333	−34.4667	2,377	2.4	268	19.7
NZG	Kermadec	Kermadec	186.6000	−23.3667	1,533	0.83	147	0.83
NZI	Kermadec	Kermadec	188.8000	−16.9000	1,918	0.62	192.5	0.65
NZE	Hikurangi	Hikurangi	182.3000	−36.0333	1,781	0.79	151.8	0.86
NZC	Hikurangi	Hikurangi	180.2000	−38.2000	1,881	1.05	168.5	1.38

For the synthetic tsunami waveforms simulation, we considered a largest modeling domain that covers the nations in the South West Pacific Ocean around the earthquake source location with a grid size of 2 arc-min (built from GEBCO14). A set of nested modeling domains were made to focus on each of the coastal gauge with grid sizes of 40, 13.333, and 4.444 arc-sec. A combination of available bathymetric data with different coverage and grid size were used for the tsunami simulation. The highest resolution bathymetric data is always used to build each modeling grid. The GEBCO14 gridded bathymetric data with grid size of 30 arc-sec was used and resampled for the largest modeling domain and smaller domains in Australia and Fiji. A bathymetric grid with resolution of 100 m (NCV100 m) is available for the area around New Caledonia and Vanuatu Roger et al., 2021). Higher resolution and quality bathymetric grids with resolution of 25 m (NCV25 m) are also available for the areas around coastal gauges in Maré (station code: MARE), Lifou (LIFO), Ouinné (OUIN), Thio (THIO), Hienghène (HIEN), Lenakel (LENA), and Port Vila (VANU). For modeling grids around New Zealand coastal gauges (AUCT, CHPT, GBIT, JACK, LOTT, MNKT, NCPT, and TAUT), a gridded bathymetric data with grid size of 10 arc-sec (NZ10sec) is available. The bathymetric data used to build the bathymetric grids around each station are shown in Table S1 in Supporting Information S1.

For tsunami threat level map creation, a nested grid configuration with four modeling domains was prepared. The largest modeling domain covers the whole Pacific Ocean with a grid size of 4 arc-min. As the main purpose of this grid setup is for tsunami threat estimate in New Zealand, other locations outside this country are only simulated using the coarsest modeling grid. The next grid level of modeling domain covers the entire of New Zealand and have grid sizes of 1 arc-min. There are two modeling domains with grid size of 15 arc-seconds, one covers New Zealand's North and South Islands and another one covers the Chatham Islands.

3. Tsunami Waveform Inversion

3.1. Tsunami Inversion Method

We first calculated two tsunami simulations using single fault models with fault parameters from the GCMT and USGS W-phase MT solutions. The simulated tsunami waveforms of these models are comparable. The trench is curved around the source area with strike angles varying from 260° to 300° based on the USGS SLAB2.0 model (Hayes et al., 2018). The trench-parallel strike angles of the focal mechanisms estimated by USGS, GCMT and Geoscience Australia are 246°, 279°, and 284°, respectively. Because the strike angle from GCMT is at the middle of these values, the strike of 279°, dip of 23°, and rake of 101° from the solution were assumed for the fault parameters in the inversion as the strike angle from the solution is at the middle of the other strike angle values (Figure 1). A fault with total length of 120 km and width of 60 km was subdivided into 6 sub-faults along strike and 3 sub-faults down dip, resulting in a sub-fault size of 20 km by 20 km. The fault dimension is consistent with that estimated by the earthquake source parameter scaling relations of Blaser et al. (2010). The top edge of the shallowest sub-faults is located along the trench at depth of 1 km.

The seafloor displacement from each sub-fault was calculated using the Okada's formula (1985). These seafloor displacement models were used as the initial modeling conditions to simulate the tsunami waveforms. The linear long wave was simulated by solving the non-dispersive linear shallow water equations with a finite difference method and a staggered leaf-frog scheme (Satake, 1995). Then a phase correction method (Watada et al., 2014) was applied to the simulated linear long wave to include the dispersion effects due to the elasticity of the earth, seawater compressibility, and the gravitational potential variation. A unit slip amount of 1 m was used to construct the tsunami Green's functions. The tsunami amplitudes at some of the coastal gauges located in near-field or far-field are about an order of magnitude larger than the amplitudes at DART stations. To treat the coastal and deep ocean tsunami waveforms equally, we weight the DART data by 50 (best value obtained after testing between 1 and 100). As fault slip must be smooth in some degree (Yabuki & Matsu'Ura, 1992), a spatial smoothness constraint was incorporated by including a smoothing matrix consisting of a Laplacian operator. The Akaike's Bayesian Information Criterion (Akaike, 1980) was used to determine the optimal value of the smoothing factor. More details for the tsunami waveform inversion algorithm used in this study, which is based on the non-negative least square method (Lawson & Hanson, 1995) are available in previous studies (i.e., Gusman et al., 2010; Gusman et al., 2015).

3.2. Fault Model Resolution and Quality

The earthquake source area is surrounded by coastal gauges and DART stations. To evaluate the source model resolution, we applied a checkerboard test (e.g., Heidarzadeh & Gusman, 2021; Lorito et al., 2010). The checkerboard pattern for the target model was made using slip amounts of 2 and 1 m (Figure 3). The target tsunami waveforms at the coastal gauges and DART stations produced using this source model were degraded by adding Gaussian noise with maximum amplitude of 1% of the clean waveform's peak amplitude. We applied the tsunami inversion code with the target waveforms to get a slip distribution. We find that the checkerboard pattern on the shallower part of the fault can be well reproduced by the inversion, but not the pattern on the deepest part (Figure 3). This is because there is no nearby station located in the main path of the tsunami energy immediately north of the source.

To measure the uncertainty of the estimated slip distribution caused by various errors associated with tsunami modeling, we ran 30 tsunami waveforms inversions with different randomly selected tsunami waveform sets at 20 out of 28 stations. The uncertainty of the estimated slip distribution is represented by the standard deviation of these 30 slip distributions.
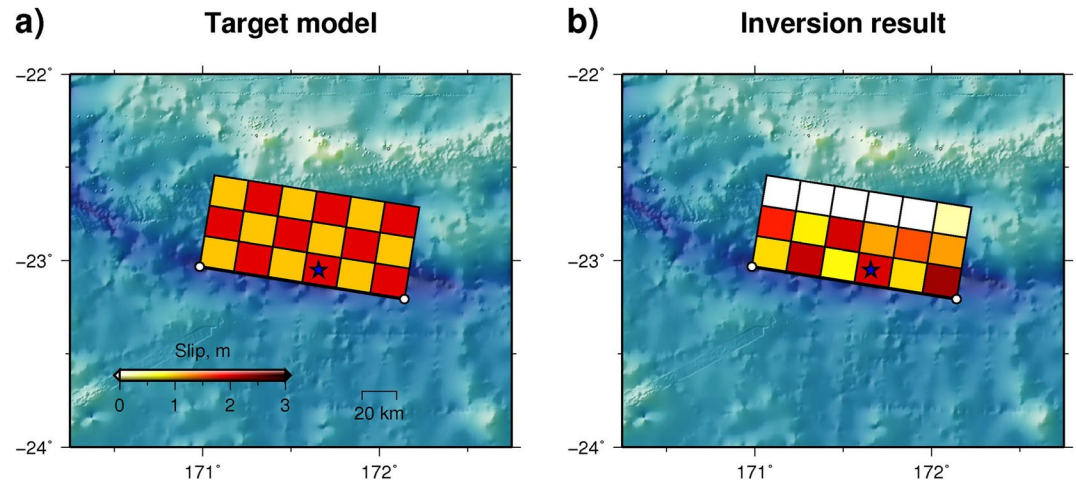
Figure 3. Checkerboard test result. (a) Target slip distribution. (b) Slip distribution obtained by an inversion using synthetic waveforms at the coastal gauges and DART stations generated from the target slip model. Slip amounts of 2 and 1 m were used to make the checkerboard pattern for the target slip model. The blue star represents the 2021 Loyalty Islands earthquake epicenter.

3.3. The Estimated Slip Distribution

An initial slip distribution estimated using only tsunami waveforms recorded at the coastal gauges is not so reliable as it has relatively large slip errors. It is difficult to accurately simulate the tsunami amplitude and arrival time at coastal gauges especially without accurate bathymetric data. Some of the coastal gauges in Vanuatu, New Caledonia, and Fiji are located inside a bay or lagoon showing complex bathymetric features potentially leading to arrival time shifts, as shown for New Caledonia and Vanuatu by Roger et al. (2021). This problem of random arrival time shifts, which may be caused by instrumental clock problems, inaccurate station positions, bay effects, harbor effects, or unknown instrument responses, can be solved by applying optimum waveform time shifts in the inversion as demonstrated in previous studies (Ho et al., 2019; Romano et al., 2016).

Tsunami waveforms at DART stations can be used in a practical way to solve the problem posed by using inaccurate simulated tsunami arrival times at coastal gauges in an inversion. DART stations are located at the deep ocean thus accurate tsunami amplitude and arrival time can be simulated using the available global bathymetric dataset. We ran an inversion to get a slip distribution using only tsunami waveforms at the four DART stations. The simulated tsunami arrival times from this estimated slip distribution were then assumed to be very close to the actual ones. Thus, any arrival time delay could be attributed to factors other than the source location, and the simulated waveforms at the coastal gauges can be used as a reference for the time shift. We found manually the optimum tsunami time shift that minimized the waveform misfit at every coastal gauge. The time shift applied to the simulated waveforms at the coastal gauges were up to 5.5 min. The tsunami waveforms at these stations were shifted: MARE (3 min), OUIN (2.58 min), THIO (4.75 min), VANU (5.5 min), HIEN (3 min), NCPT (3 min), TAUT (4.6 min), and PKEM (3 min). The final slip distribution was obtained from tsunami waveforms at both coastal gauge and DART stations with the optimum time shift applied to the coastal gauges based upon the simulated waveforms.

Ideally, the first cycle of the tsunami waveform is the only part of the wave that should be used in a tsunami waveform inversion, as it contains mostly information about the source while the later waves tend to be more affected by coastal geomorphology. Unfortunately, for some stations the first tsunami wave cycle is too small or too unclear to be used in this way. To make this data useful, more wave cycles can be included in the inversion as long as doing so does not significantly deteriorate the waveform fits at the other stations that use only the first wave cycle. In this case, we used two or three wave cycles at LIFO, NUMBO, VANU, KJNI, LITZ, GBIT, PKEM, and CHST, and a wave envelope at OUVE.

The estimated slip distribution has a major slip region near the trench (Figure 4a). This is consistent with the USGS finite fault model (Figure 4a) which was estimated from 17 teleseismic broadband P waveforms, 7 broadband SH waveforms, and 29 long period surface waves (USGS, 2021). The maximum slip amount estimated
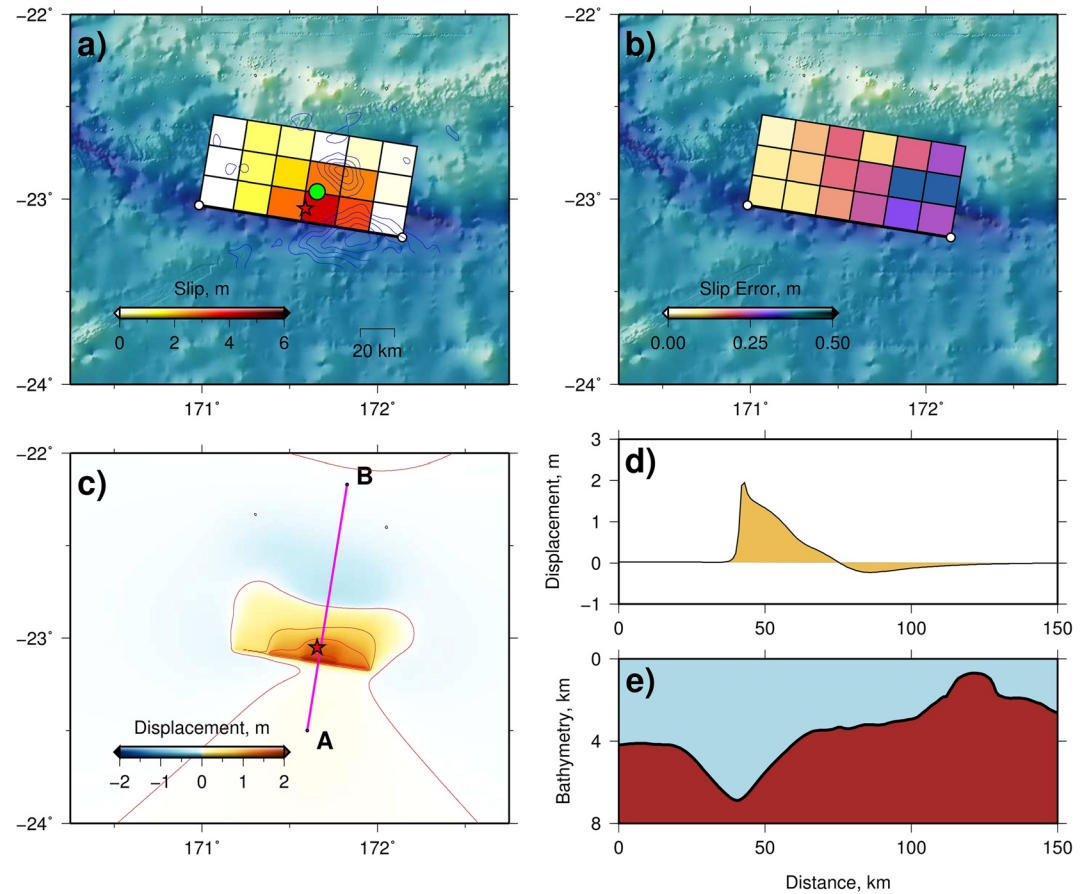
Figure 4. (a) Slip distribution for the 2021 Loyalty Islands earthquake estimated by tsunami waveform inversion using tsunami waveforms recorded at coastal gauges and DART stations. Blue lines represent the USGS finite fault model contours at 1 m intervals, the red star represents the epicenter and the green circle represents the GCMT centroid location. (b) Slip error map for the estimated slip distribution. (c) Calculated co-seismic seafloor vertical displacement from the estimated slip distribution. The vertical displacement contour interval is 0.5 m. The purple line indicates cross-section A-B. (d) The estimated co-seismic seafloor vertical displacement profile along cross-section A-B. (e) Bathymetric profile along cross-section A-B.

in this study is 4.1 m (Figure 4a and Table 2). The estimated maximum uplift near the trench is 2.1 m and the subsidence is 0.24 m (Figures 4c and 4d). While the calculated tsunami energy potential from the estimated sea surface displacement is 7.87×10^{12} J.

The calculated seismic moment from the slip distribution, assuming a rigidity of 40 GPa (e.g., Fujii & Satake, 2008; the USGS fault model of this event), is 3.39×10^{20} Nm or equal to Mw 7.65. This estimated seismic moment is smaller than the values from the GCMT solution of 4.01×10^{20} Nm (16% smaller) and from the USGS fault model of 4.4×10^{20} Nm (23% smaller). An inversion using only DART data which are relatively far away from the source and span a narrow azimuth range to the east gives a smaller calculated seismic moment of 3.05×10^{20} Nm. The use of data at near-field coastal gauge stations brings the estimated moment closer to the one from GCMT.

The estimated slip distribution results in tsunami waveforms that largely reproduce the detailed wave-shapes in the inverted window at LENA, LIFO, OUIN, THIO, OUVE, LEVU, LITZ, GBIT, LOTT, GCSB, PKEM coastal gauges and all DART stations (Figure 5). At HIEN, KJNI, LUGA, UPOL, JACK stations, the upper or lower bound on the amplitude of the overall signal are adequately reproduced. However, the fits at NUMBO, VITI, NCPT, AUCT, TAUT, MARE, VANU, and LUGA are very poor, which is probably attributable to complex and poorly represented bathymetry in the proximity of the gauges.

The uncertainty or error for the estimated slip distribution was calculated from the 30 inversions that were made with random combinations of stations. For the sub-fault with the largest slip (4.1 m), the error of the estimate is

Table 2
Fault Parameters and Slip Amounts From the Tsunami Waveform Inversion

Center lon (deg)	Center lat (deg)	Length (km)	Width (km)	Depth (km)	Strike (deg)	Dip (deg)	Rake (deg)	Slip (m)	Error (±m)
172.0595	−23.1109	20	20	4.9	279	23	101	0	0.25
171.8663	−23.0820	20	20	4.9	279	23	101	3.12	0.29
171.6732	−23.0532	20	20	4.9	279	23	101	4.14	0.23
171.4800	−23.0243	20	20	4.9	279	23	101	2.8	0.16
171.2868	−22.9954	20	20	4.9	279	23	101	1.1	0.09
171.0936	−22.9666	20	20	4.9	279	23	101	0	0.08
172.0876	−22.9472	20	20	12.7	279	23	101	0.14	0.37
171.8944	−22.9184	20	20	12.7	279	23	101	2.6	0.37
171.7013	−22.8895	20	20	12.7	279	23	101	2.71	0.22
171.5081	−22.8607	20	20	12.7	279	23	101	1.79	0.19
171.3149	−22.8318	20	20	12.7	279	23	101	0.92	0.13
171.1217	−22.8029	20	20	12.7	279	23	101	0	0.08
172.1157	−22.7836	20	20	20.5	279	23	101	0.09	0.26
171.9225	−22.7547	20	20	20.5	279	23	101	0.31	0.21
171.7293	−22.7259	20	20	20.5	279	23	101	0.01	0.11
171.5361	−22.6970	20	20	20.5	279	23	101	0.61	0.2
171.3430	−22.6682	20	20	20.5	279	23	101	0.88	0.14
171.1498	−22.6393	20	20	20.5	279	23	101	0	0.05

±0.2 m or about 6% of the slip amount, which is very low. Higher error percentages for the sub-faults exist mainly on the eastern part of the fault model. The error distribution can be seen in Table 2 and Figure 4b. Overall, the reliability of the estimated major slip region is high with very low slip errors. This error estimate and also the checkerboard test result (Figure 3) show that the inversion result in the shallow region where the major slip region is located, is well constrained and resolved by the station coverage. For this case the uncertainty of the estimated slip on the deepest sub-faults from the tsunami data is high. This uncertainty and our estimated seismic moment being smaller than the estimations from seismic data imply that there is a possibility of underestimation of the slip amount on the deepest sub-faults in our model, which may not be particularly tsunamigenic.

4. Seismic Wave Simulation

4.1. Methodology

To evaluate the slip distribution estimated from the tsunami data, we compare observed and synthetic seismograms at Global Seismographic Network stations using Specfem3D_Globe which is a spectral element wave propagation code (Komatitsch & Tromp, 2002a, 2002b), with a 3D global tomographic model consisting of crustal velocity model Crust2.0 (Bassin et al., 2000), mantle model S40RTS (Ritsema et al., 2011) and 1-D PREM radial attenuation. The effect of the spherical earth, ocean loading, topography, gravity, rotation and anelastic attenuation that potentially influence long-period surface waves was included in the simulation. We used a finite fault approach (e.g., Hjörleifsdóttir et al., 2009; Holden et al., 2017) where a set of point sources represent the spatiotemporal evolution of slip on the faults. Synthetic seismograms were numerically well resolved down to 20 s. We used a dataset from a total of 21 stations to quantify the model accuracy by a data-synthetic misfit defined as

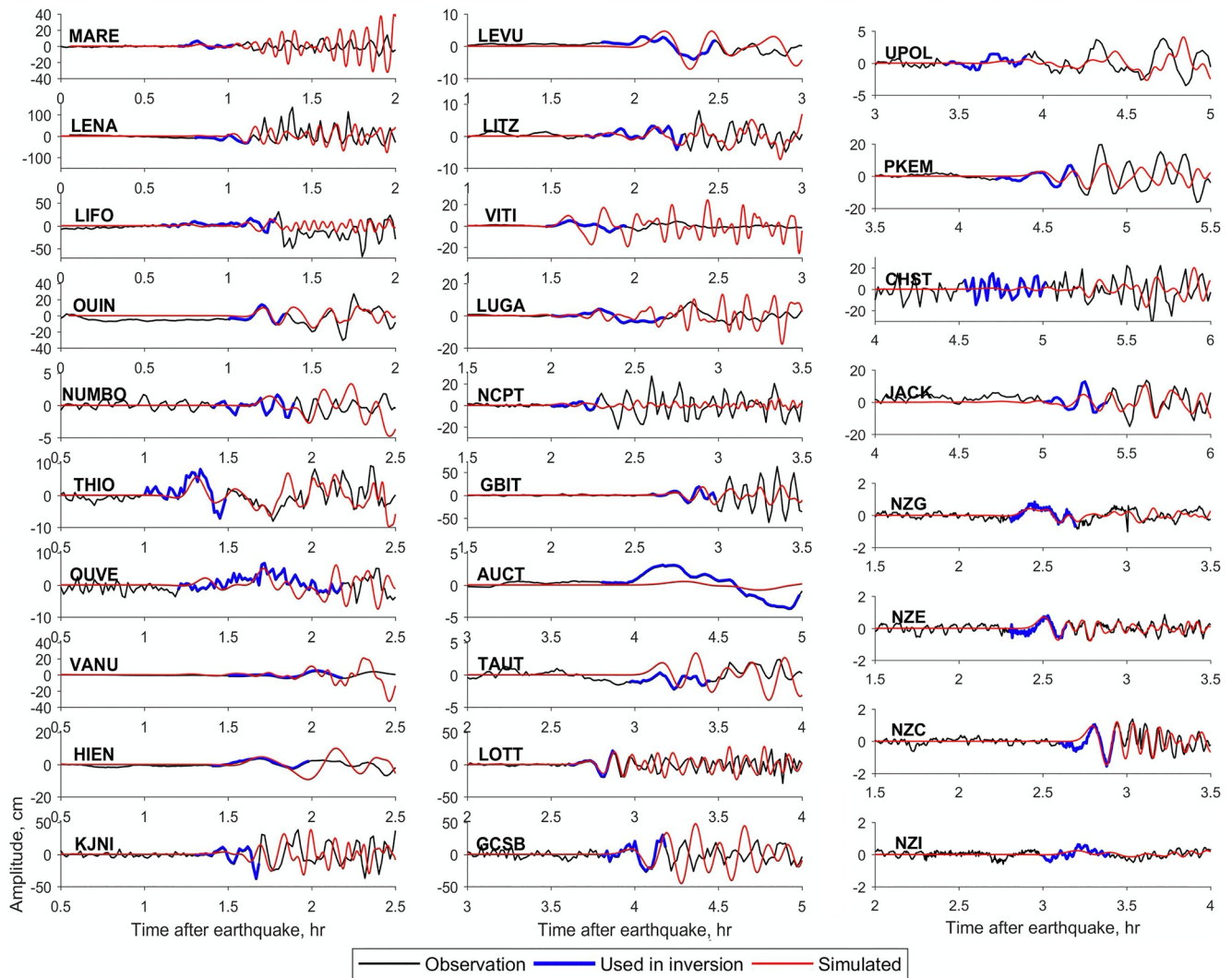$$\chi_{full} = \sum \frac{|d - s|^2}{|d||s|} \tag{1}$$

Figure 5. Comparison between the observed (black) and simulated (red) tsunami waveforms. Blue lines indicate the recorded waveforms that were used in the inversion.

where s and d are the amplitude of the vertical component of observed and synthetic displacement seismogram, respectively, and the summation was performed over all stations (e.g., Gusman, Kaneko, et al., 2020). To consider an alternative misfit quantification, we also report peak amplitude misfit defined as

$$\chi_{peak} = \sum \frac{|\max(d) - \max(s)|^2}{|\max(d)||\max(s)|} \tag{2}$$

Here we evaluate our static slip distribution estimated from the tsunami data using seismic wave simulations. Since seismic waves are sensitive to the rupture velocity, we ran simulations with assumed constant rupture velocities of 1.0, 1.5 and 2.0 km/s. We did not consider slower rupture velocities (<1.0 km), as assuming 0.5 km/s leads to the source duration of >200 s, which deviates significantly from the shorter (<100 s) duration of the GCMT or USGS finite fault model. We also note that the 2021 Loyalty Islands earthquake is not a tsunami earthquake that sometimes results in very slow rupture velocities (~0.5 km/s) and efficiently excites large tsunamis (e.g., Kanamori, 1972; Riquelme & Fuentes, 2021). The assumed rise time for each subfault was based on the half duration (*hdur*) of the Gaussian moment rate function calculated by the following equation (Ekström et al., 2012):

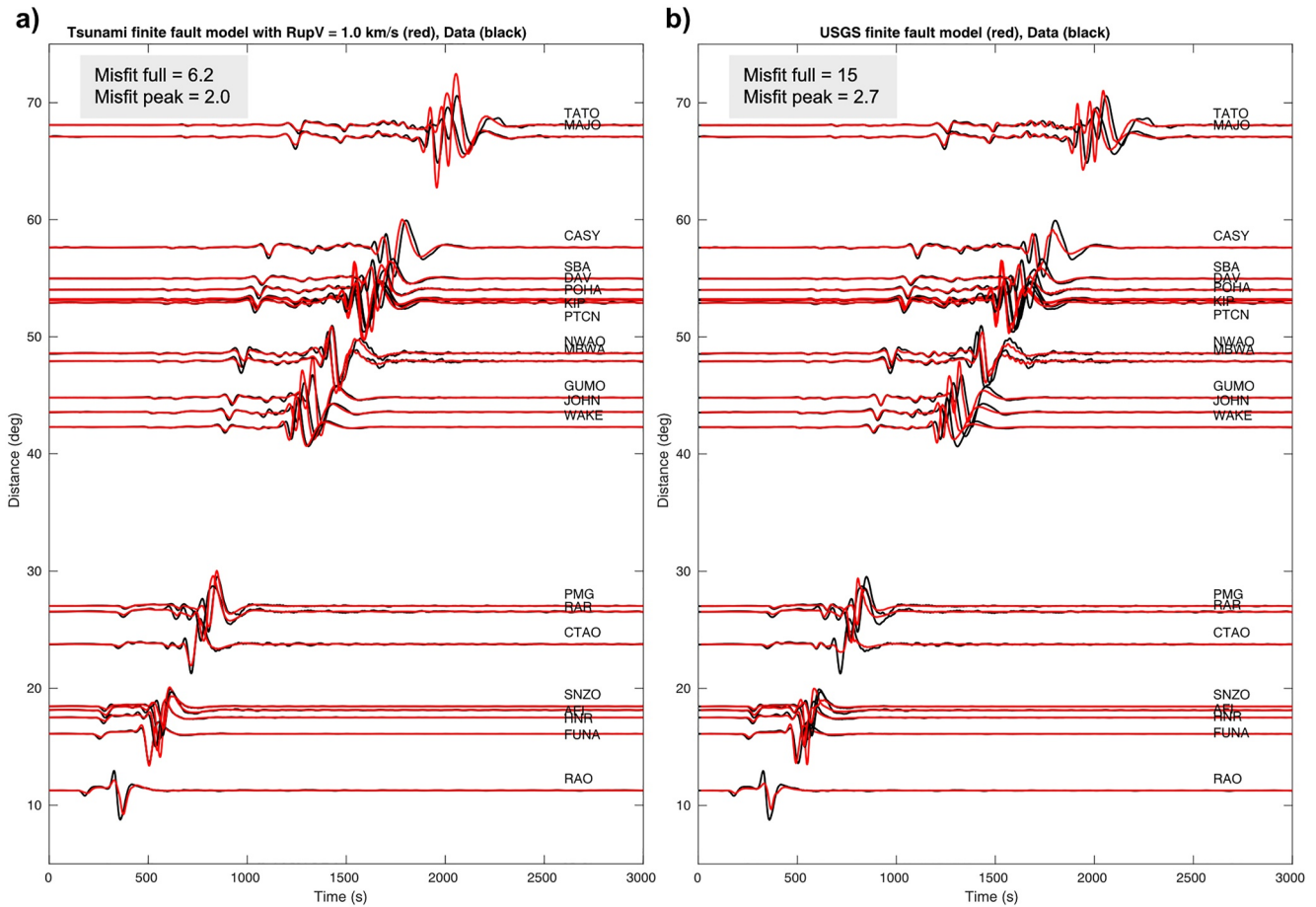$$hdur = 1.05 \times 10^{-8} \times \left(M_o \times 10^7\right)^{1/3} \tag{3}$$

Figure 6. Seismic simulation results using (a) our finite fault model estimated from tsunami waveforms with an assumed rupture velocity of 1.0 km/s, and (b) the USGS finite fault model. Observed (black) and simulated (red) vertical displacement waveform band-pass-filtered between 50 and 500 s are shown. For each trace, the amplitude is normalized by the maximum amplitude of the data at the corresponding station.

For comparison, we also simulated the seismic waves using the GCMT solution and the USGS finite fault models. For all the source scenarios, the seismic waves were compared within a period band of 50–500 s.

4.2. Simulation Results

The seismic waves can be best reproduced with the estimated slip distribution using an assumed rupture velocity of 1.0 km/s (Figure 6a). The calculated full waveform misfit and peak amplitude misfit using Equations (1) and (2) for this model are 6.2 and 2.0, respectively (Figure 6a). The full waveform and peak misfits from the model with a rupture velocity of 1.5 km/s are 15 and 4.7, respectively (Figure S1 in Supporting Information S1), while those using a rupture velocity of 2.0 km/s are 21 and 6.7, respectively (Figure S2 in Supporting Information S1). The misfit values for the GCMT solution ($\chi_{full} = 21$, $\chi_{peak} = 8.2$) (Figure S3 in Supporting Information S1) and the USGS finite fault model ($\chi_{full} = 15$, $\chi_{peak} = 2.7$) (Figure 6b) are larger than the ones for the best tsunami source model (Figure 4a). These results suggest that this tsunami source model can reproduce well the seismic waves within the considered period band, even though the calculated seismic moment of the tsunami source model is smaller than those from GCMT solution and USGS source model.

As mentioned in the previous section, the slip on the deepest sub-faults in the tsunami source model might be underestimated. To evaluate the potential slip on the deepest sub-faults, we increase the slip amount on these sub-faults to make the calculated seismic moment match the GCMT one and then run the seismic wave simulation with an assumed rupture velocity of 1.0 km/s (Figure S4 in Supporting Information S1). The overall misfit from this model is only slightly larger ($\chi_{full} = 5.9$, $\chi_{peak} = 2.6$) than the best tsunami source model, suggesting that the

Table 3
Tsunami Threat Levels in New Zealand With Their Tsunami Height Thresholds, Color Codes, Descriptions and Threat Level Names for Dissemination

Threat level	Tsunami amplitude	Color	Description	Threat level for dissemination
0	$h \leq 0.3$ m	White	No threat	No threat
1	$0.3 < h \leq 1$ m	Green	Threat to beach and small boats	Beach and Marine threat
2	$1 < h \leq 3$ m	Light blue	Some land threat	Land and Marine threat
3	$3 < h \leq 5$ m	Blue	Moderate land threat	
4	$5 < h \leq 8$ m	Pink	High land threat	
5	$h > 8$ m	Purple	Severe land threat	

discrepancy in the seismic moment between the tsunami source model and GCMT is due to the slip on the deep subfaults which the tsunami data are insensitive to.

5. Tsunami Forecasting for New Zealand

The COMCOT (Cornell Multi-Grid Coupled Tsunami model) program (Liu et al., 1998; Wang & Liu, 2006; Wang & Power, 2011) was used to make the database of tsunami threat level maps for New Zealand. The computer program was used to simulate tsunami generation and propagation from their sources to New Zealand coasts. A simulation time of 30 hr of tsunami propagation was considered to ensure that maximum tsunami amplitudes were obtained. We used the New Zealand eScience Infrastructure (NeSI) high performance computing facilities to run the simulations. The CPU time required to complete one simulation is about 3 days. The nonlinear shallow water equations were solved to simulate the tsunami. Vertical wall boundaries were implemented by assuming any grid cell with an elevation larger or equal to −10 cm to be land.

The New Zealand coast is divided into 43 tsunami warning regions (NEMA, 2020) (Figure S5 in Supporting Information S1). There are six levels of tsunami threat in New Zealand, which are based on the shoreline tsunami amplitude (Table 3). However, for tsunami warning dissemination, the threat levels are also grouped into three categories (Table 3), which are No Threat, Beach and Marine Threat, and Land and Marine Threat. For each earthquake scenario, the 99th percentile of all shoreline (grid cells adjacent to wall boundary) tsunami amplitudes within each warning region is calculated and then used to identify the tsunami threat level. The value for the 99th percentile is used instead of the maximum value to avoid outliers.

5.1. Tsunami Threat Levels From the Estimated Fault Slip Distribution

The tsunami simulation from the estimated fault slip distribution categorizes many tsunami warning regions as being under Beach and Marine Threat, and no region is under the Land and Marine Threat. The warning regions that should be under the Beach and Marine Threat according to that source include the West Coast of the North Island from Cape Reinga to Kaipara Harbor, and from Mokau to Hawera; the East Coast of the North Island from Cape Reinga to Waihi Beach excluding the East Coast of Auckland, and from Matata to Mahia; and the West Coast of the South Island from Farewell Spit to Milford Sound (Figure 7a). The other coastal regions are under No Threat. However, it should be noted that the procedure described here for determining the tsunami threat levels from an estimated source model is challenging during an event. The complexity of tsunami waveform inversion and the many hours required for simulating the tsunami on high resolution grids using the source model are the main drawbacks. Real-time operationalization of an inversion-based forecasting approach can be improved with simplification of the problem including possibilities of more coarsely defining the finite fault earthquake model and using empirical shoreline tsunami amplitude equations to approximate coastal threat zones. Running the tsunami simulation to make a threat level map on the fly during an event is not feasible as the CPU time for the desired modeling setup described above even using NeSI HPC was about 3 days. However, recent developments of GPU-based tsunami numerical models (e.g., Furuyama & Maihara, 2014; Nagasu et al., 2017) showed that the simulation time can be significantly reduced. In this study, the threat level map from the estimated source model is used purely as reference to evaluate the forecast based on the pre-computed scenarios. During the response, the
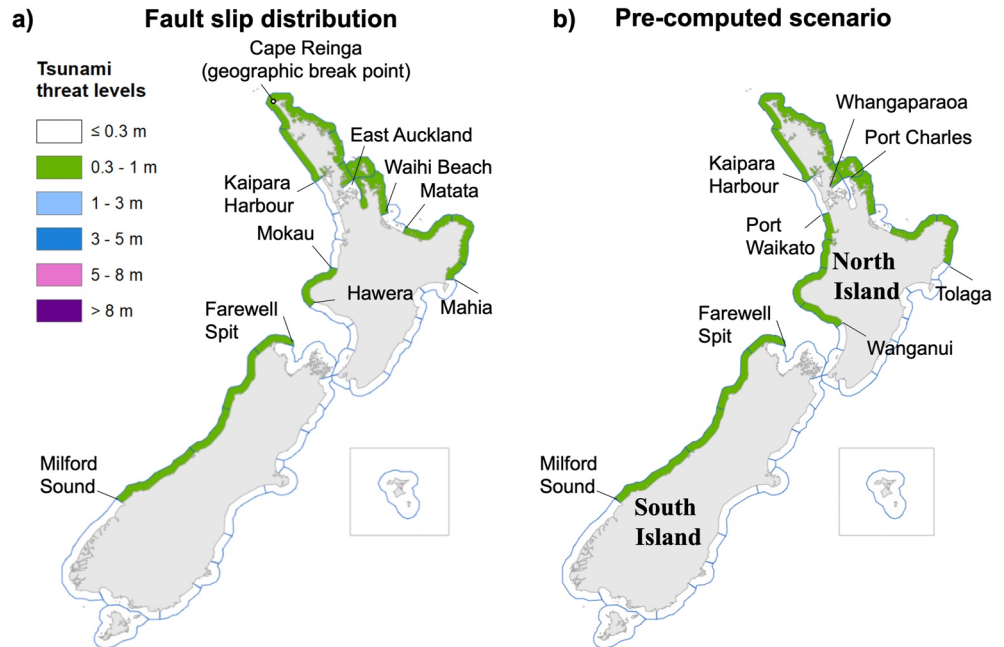
Figure 7. Tsunami threat level maps for New Zealand from (a) a computation using the estimated fault slip distribution of the 2021 Loyalty Islands earthquake and (b) a pre-computed earthquake scenario (Mw 7.7) that best matches the epicenter and magnitude of the earthquake. The threat level was determined from the 99th percentile of the simulated tsunami amplitudes within each warning region.

New Zealand Tsunami Expert Panel (NZTEP) used a coarse simplification to adjust forecasts, described further in Section 6.3.

The amplitude of the first observed tsunami wave cycle can be much smaller than the maximum observed tsunami amplitude at coastal gauges. As an example, the amplitude of the first wave at NCPT (North Cape) station is only 4 cm while the maximum amplitude recorded by the same station is 29 cm. The complete list of the observed first wave cycle amplitudes and the maximum amplitudes at the stations can be seen in Table 1. This emphasizes that the simulation time should be set long enough to capture the maximum simulated tsunami amplitude.

Several coastal zones in the South Island are identified by this method as being under the Beach and Marine Threat with tsunami larger than 0.3 m. The observed first tsunami wave cycle amplitude in Jackson Bay which is located in the West Coast region of South Island is 13 cm, while the maximum amplitude is 35 cm which validates the tsunami threat level from the estimated fault slip distribution. Both simulation and observation at Jackson Bay show that the tsunami is even higher than in some of the stations in the North Island (Figure 8b and Table 1). Bathymetric features, and especially the Challenger Plateau and Bellona Basin (Uruski, 2010), allow the tsunami to focus part of its energy on the West Coast of the South Island as shown by the snapshots of the tsunami propagation in Figure 8a and the maximum tsunami amplitude distribution in Figure 2. The part of the tsunami propagating over the deeper Bellona Basin goes with a faster speed than the part propagating over the neighboring shallower Challenger Plateau: the tsunami front slows down when arriving on the northwesternmost part of the Challenger Plateau, wrapping around the set of seamounts in the area around 38°S, 167°E (Rowden et al., 2005) and concentrating the energy at the back of the seamounts, with a trajectory still oriented toward the West Coast of the South Island but with higher amplitudes. In addition, numerous submarine canyon complexes located along the southwestern margin of the Challenger Plateau (Neil et al., 2015) act as waveguides to focus tsunami waves on specific locations and can also explain the higher waves recorded at Jackson Bay (Figure 8b).

5.2. Tsunami Threat Levels From a Nearest Pre-Computed Scenario (Uniform Slip Model)

Earthquake scenarios in subduction zones around the Pacific Ocean were used to build a database of tsunami threat level in New Zealand. The size of the fault patches used for the earthquake scenarios in the Vanuatu
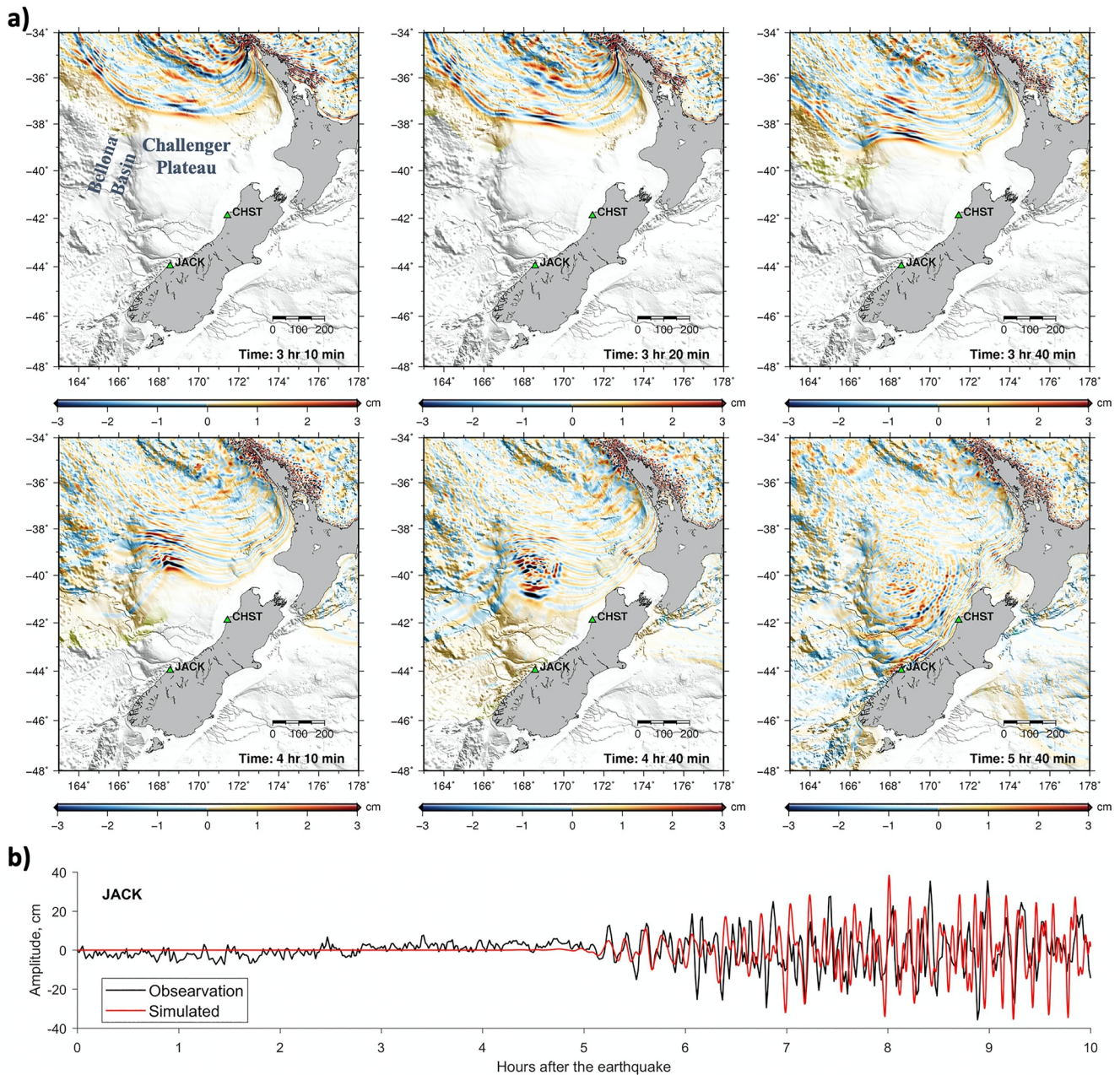
Figure 8. (a) Simulated tsunami propagation snapshots from the 2021 Loyalty Islands earthquake source model over Bellona Basin and Challenger Plateau near New Zealand. Green triangles indicate the locations of JACK and CHST coastal gauges. (b) Observed tsunami waveforms at JACK (Jackson Bay) coastal gauge.

subduction zone is 50 km long and 25 km wide. The earthquake scenario moment magnitudes (Mw) are ranged from 6.9 to 9.3, with magnitude interval of 0.2, and are a combination of fault patches. The distance between the scenario's epicenters for magnitudes 7.5, 7.7, and 7.9 is 150 km. The assumed fault parameters and orientations for the fault models in this region are based on fault patches developed by the U.S. National Oceanic and Atmospheric Administration (NOAA) (Gica, 2008) and those available from Power et al. (2012). An earthquake scenario in the Vanuatu subduction zone with a moment magnitude of 7.7 that is the nearest to the 2021 Loyalty Islands earthquake epicenter was selected from the database. This scenario epicenter is ~70 km westward the actual epicenter. The uniform slip earthquake scenario has four fault patches and a slip amount of 2.2 m (Table 4).

The predicted threat levels at most of the coastal regions (38 out of 43 regions) matched the reference ones (Figure 7). Just like the threat level map from the fault slip distribution, the one from the pre-computed scenario

Table 4
Fault Parameters of the WestMw7.7 and EastMw7.7 Scenarios Selected From the Database (the Original Scenario Names in the Database Are NBSV_Pt8_Mw7.70 and NBSV_Pt9_Mw7.70, Respectively)

Center top lon (deg)	Center top lat (deg)	Length (km)	Width (km)	Depth (km)	Strike (deg)	Dip (deg)	Rake (deg)	Slip (m)
WestMw7.7 (NBSV_Pt8_Mw7.70)								
170.6785	−23.0542	50	25	5	295.6	21.3	90	2.2
170.7604	−22.8943	50	25	14.1	295.6	21.3	90	2.2
171.1714	−23.2182	50	25	5	286.1	20.4	90	2.2
171.2262	−23.0377	50	25	13.7	286.1	20.4	90	2.2
EastMw7.7 (NBSV_Pt9_Mw7.70)								
172.4005	−23.2771	50	25	5	268.2	27.8	90	2.2
172.3939	−23.085	50	25	16.6	268.2	27.8	90	2.2
172.9715	−23.2238	50	25	5	261.8	30.9	90	2.2
172.9419	−23.0334	50	25	17.8	261.8	30.9	90	2.2

has no warning region that should be under the Land and Marine Threat (Figure 7b). The warning regions that should be under the Beach and Marine Threat include the West Coast of the North Island from Cape Reinga to Kaipara Harbor, and from Port Waikato to Wanganui; the East Coast of the North Island from Cape Reinga to Waihi Beach excluding the region from Whangaparaoa to Port Charles, and from Matata to Tolaga Bay (Figure 7b). While the threat levels for the warning regions in the South Island from the two models are the same. The selected pre-computed scenario underestimated the tsunami threat in two warning regions by one level lower and overestimated the threat in three warning regions by one level higher.

5.3. Interpolated Tsunami Threat Levels From Pre-Computed Scenarios (Uniform Slip Models)

The tsunami from the earthquake can be approximated by interpolating simulation results from scenarios located around the epicenter (e.g., Tatehata, 1997). Here we interpolated the threat level maps from these two scenarios with the inverse distance weighting method (Shepard, 1968). A general way of finding an interpolated tsunami threat level (f_i) in the 43 warning regions ($i = 1, 2, …, 43$) for a given epicenter based on pre-computed tsunami threat level in the database $f_{i,j}$ for $j = 1, 2, …, Ns$ is to use the following equation:

$$f_i = \begin{cases} \dfrac{\sum_{j=1}^{Ns} w_j \cdot f_{i,j}}{\sum_{j=1}^{Ns} w_j}, & if\ d \neq 0\ for\ all\ j, \\ f_{i,j}, & if\ d = 0\ for\ some\ j, \end{cases} \tag{4}$$

where

$$w_j = \frac{1}{d^p} \tag{5}$$

d being the distance between the earthquake epicenter and scenario epicenter (reference point), Ns the number of scenarios which is 2 in this case, and p the power parameter set to 1.

As mentioned above, the reference point or epicenter of the pre-computed scenario is westward the actual epicenter. We produced a threat level map by interpolating the tsunami heights in the warning zones from the nearest pre-computed scenario with Mw7.7 located west of the epicenter (West Mw7.7 described in Section 5.2) and the second nearest pre-computed scenario with also Mw7.7 located east of the epicenter (East Mw7.7) (Table 4). Figure 9 shows the vertical displacements (a, b) and maximum tsunami amplitude distributions (c, d) from these two scenarios. The interpolation result shows that there is one warning region which is the North Cape
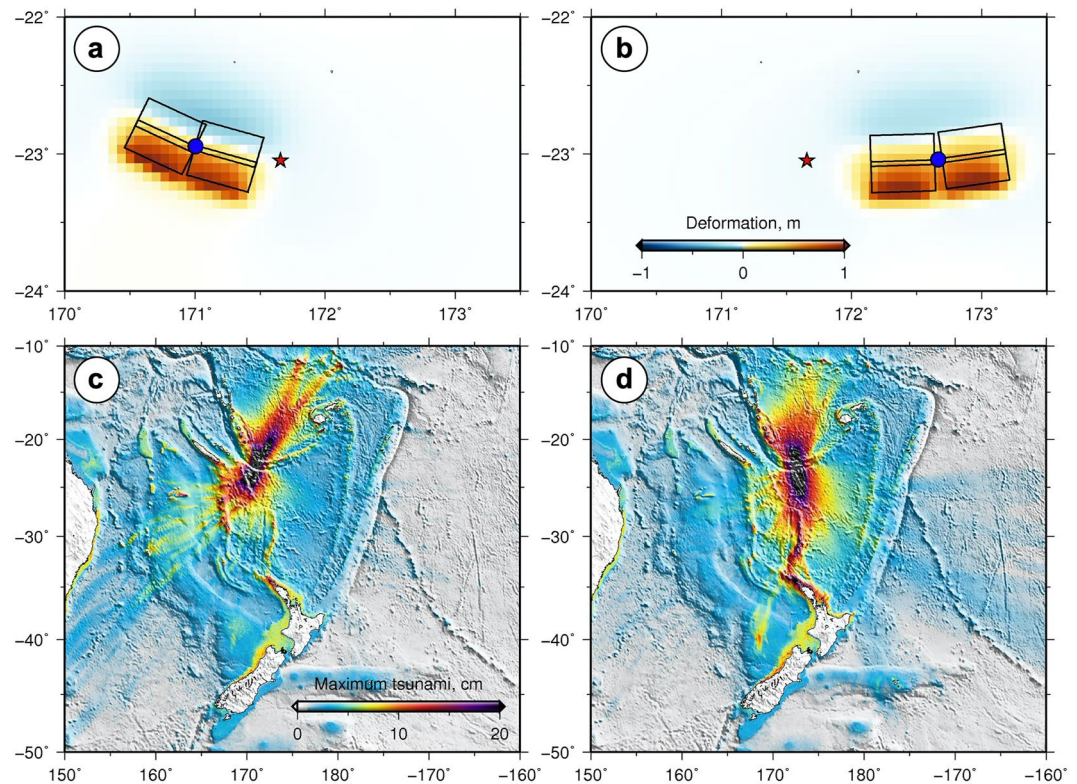
Figure 9. Initial tsunami simulation of seafloor displacements and simulated tsunami amplitude distributions for the (a and c) WestMw7.7 uniform slip scenario (nearest scenario) and (b and d) EastMw7.7 uniform slip scenario. Black rectangles indicate the fault patches used by the scenario. The blue star represents the earthquake epicenter, while the blue dot represents the reference point/epicenter for the scenario.

area from Ahipara to Bay of Islands (Figure 10a) that should be under the Land and Marine Threat, while there is no region under this threat category from the previous two models. The warning region from Waihi beach to Matata should be under No Threat according to the reference map (Figure 7a), which is a level lower than the one according to the interpolation result (Figure 10a). While the threat levels for the other warning regions are the same as those in the selected pre-computed scenario.

The interpolated threat levels (Figure 10a) at most of the coastal regions (36 out of 43 regions) matched the reference ones (Figure 7a). Based on the reference threat level map, the interpolated scenario underestimated the tsunami threat in two warning regions by one level lower and overestimated the threat in five warning regions by one level higher. This makes the forecast accuracy from the interpolation result slightly worse than the one from the pre-computed scenario nearest to the epicenter. The interpolated threat levels are overall slightly higher than the one from the nearest pre-computed scenario. The tsunami height values for the warning regions from different models can be seen in Table S2 in Supporting Information S1. The warning levels are overestimated because the earthquake source model that was used to make the reference map has a slightly smaller seismic moment (Mo = 3.39×10^{20} Nm equivalent to moment magnitude Mw7.65) than the pre-computed scenario one (Mo = 4.4×10^{20} Nm or Mw7.7). Similarly, the tsunami potential energy from the reference model (7.87×10^{12} J) is 20% smaller than the one from the scenario (9.78×10^{12} J).

6. Discussion

6.1. Toward Improved Real-Time Update of Tsunami Threat Level Maps

The tsunami forecast using pre-computed scenario database approach may not be enough if it only relies on the earthquake magnitude estimate. Tsunami records at coastal gauges and DART stations can be used to confirm or update the tsunami threat level. For this event, the tsunami arrived in the North Cape of New Zealand
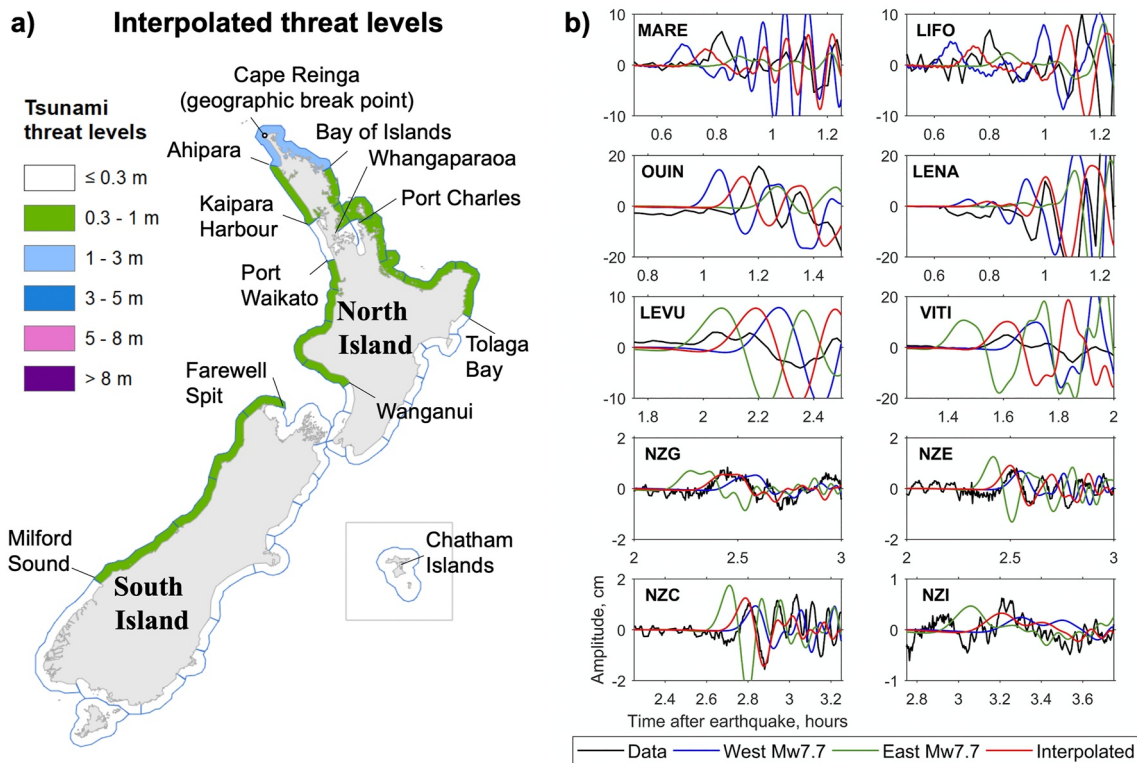
Figure 10. (a) Threat level map obtained by interpolating the results from two Mw7.7 scenarios nearest to the epicenter. (b) Observed, simulated and interpolated tsunami waveforms. Red lines indicate the interpolated tsunami waveforms from tsunami waveforms of the pre-computed scenario Mw7.7 located west of the epicenter (blue lines) and those of a second nearest scenario Mw7.7 located east of the epicenter (green lines). The locations of the scenarios are shown in Figures 9a and 9b.

approximately 2 hr after the earthquake. Within 1.5 hr after the earthquake, at least one complete tsunami wave cycle had been recorded at four coastal gauges (MARE, OUIN, LIFO, and LENA) located in the azimuthal quadrant west-northwest of the epicenter. The sea level recorded within 2 hr after the earthquake at LEVU and VITI which are located in Fiji to the east of the epicenter can be used to evaluate the tsunami. While the tsunami arrival times at the two closest DART stations (NZG and NZE) are approximately 2.5 hr after the earthquake. We note that recent network expansion (July 2021) provides three additional DART stations within one-hour travel time of this earthquake source (Burbidge & Roger, 2022). When complete, the array is designed to detect events originating from any Hikurangi/Kermadec/Tonga/Vanuatu trench source within 30 min. Any warning update for this event based on the February 2021 operational DART stations network would be too late for first wave arrival at North Cape but could be valuable prior to maximum wave arrivals and also for dynamic forecasting during the latter stages of the threat, supporting staggered de-escalation. This shows the relevance of the additional DART stations (Power et al., 2018) recently deployed around the Vanuatu subduction zone (DART NZJ, K, and L) to enable a rapid characterization of any tsunami generated in this area that threaten New Zealand and the nearby islands.

The existing pre-computed tsunami waveforms at coastal gauges outside New Zealand were simulated using a low-resolution modeling grid (4 arc-min) as explained in Section 2.2. To make the observed tsunami waveform at coastal gauges more useful in validating or updating a tsunami warning, the pre-computed tsunami waveforms need to be obtained using high resolution grids (Figure 10b). In this study we simulated the tsunamis at coastal gauges with our highest modeling grid resolution for the two uniform slip scenarios (West Mw 7.7 and East Mw 7.7) located around the actual epicenter (Figures 9a and 9b).

The tsunami waveforms from these two scenarios can be interpolated to get the estimated tsunami waveforms for the event (Figure 10b). We used a waveform interpolation method (Wang et al., 2019) which is based on the Huygens-Fresnel principle. Equations (4) and (5) can be modified and then used to interpolate the tsunami arrival times and amplitudes for an interpolated event. First, we estimated the arrival time at the stations for
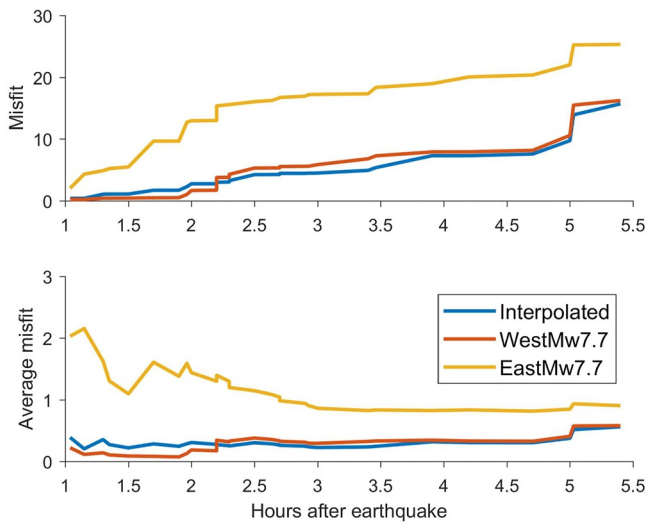
Figure 11. Misfit and average misfit of tsunami amplitude at observation stations from the interpolated, WestMw7.7, EastMw7.7 scenarios. The misfit is increasing over time as the number of stations used for the calculation increases. The average misfit is the misfit divided by the number of stations.

the interpolated event. The interpolated arrival time at kth station of t_k^{arr} is calculated from the simulated arrival time from the scenarios $t_{k,j}^{arr}$ using the following equation:

$$t_k^{arr} = \frac{\sum_{j=1}^{Ns} w_j \cdot t_{k,j}^{arr}}{\sum_{j=1}^{Ns} w_j} \tag{6}$$

The simulated arrival time of each scenario is marked when the amplitude of the simulated tsunami at the station reached a threshold. The thresholds for coastal gauges are >1 cm while that for DARTs is 0.1 cm. Then the tsunami waveforms (y_k) can be interpolated from the amplitudes of the two simulated waveforms ($Y_{k,j}$) using the following equation:

$$y_k \left(t - t_k^{arr} \right) = \frac{\sum_{j=1}^{Ns} w_j \cdot Y_{k,j} \left(t - t_{k,j}^{arr} \right)}{\sum_{j=1}^{Ns} w_j} \tag{7}$$

The interpolated tsunami waveforms fit better the observations in term of both amplitude and arrival time compared to those from the two nearest Mw7.7 scenarios as shown in Figure 10b. At coastal gauges located west of the epicenter such as MARE, LIFO, OUIN, and LENA, the West Mw7.7 scenario tsunami arrived earlier than the observation, and the East Mw7.7 scenario tsunami arrived after the observed arrival time. At station located east of the epicenter such as LEVU and VITI coastal gauges and the DARTs, the East Mw7.7 scenario tsunami arrived earlier than the observation, and the West Mw7.7 scenario tsunami arrived after the observed arrival time. While the interpolated waveforms arrived almost at the same time as the observations. To evaluate the scenarios the tsunami waveforms misfits are calculated. The amplitude data-simulation misfit of the peak amplitudes for the interpolated ($\chi_{peak} = 15.7$) and WestMw7.7 ($\chi_{peak} = 16.2$) tsunami waveforms are very similar, and these values are much smaller than 25.3 from EastMw7.7 scenario (Figure 11). Some selected waveforms used to calculate these misfits can be seen in Figure 10b.

In retrospect, after the earthquake moment magnitude became available, we had two tsunami threat level maps. One was from the scenario nearest to the epicenter and the other was an interpolated threat level map from two scenarios nearest to the epicenter. To make a conservative tsunami forecast, the higher threat level at each warning zone from the two scenarios should be selected. The tsunami waveforms recorded within 1.5 hr at the nearby four coastal gauges showed that the interpolated scenario has tsunami waveforms with better tsunami arrival time but slightly worse tsunami amplitude predictions ($\chi_{peak\_1.5hrs} = 1.09$) compared to those from the nearest scenario to the epicenter ($\chi_{peak\_1.5hrs} = 0.42$) (Figure 11). The analysis with more tsunami waveforms at DART stations and coastal gauges that were available more than 2.2 hr after the earthquake suggest that the best scenario was the interpolated scenario which has a smaller misfit (Figure 11) and better tsunami arrival time prediction.

6.2. Expanding the Scenario Database

The current tsunami threat level maps for New Zealand are all based on thrust earthquake scenarios. The 2021 Loyalty Islands earthquake was also a thrust event. The magnitude and focal mechanism of the earthquake can be confidently concluded in about 2 hr before the tsunami reaches any New Zealand coastline or 30 min after the earthquake occurred. However, initial earthquake magnitude estimates for unusual kinds of tsunamigenic earthquakes such as tsunami earthquakes (Kanamori, 1972) may not be accurately obtained as quickly as those of typical thrust faulting earthquakes. Further real-time analysis using W-phase inversion, source duration, source spectrum, and P coda excitation can provide rapid measures to indicate if an event is likely to have unusual shallow slip properties associated with higher tsunami excitation than for other events of the same magnitude (Bell et al., 2014; Bilek & Lay, 1999; Kanamori & Rivera, 2008; Newman et al., 2011; Satake et al., 2013). To complement a real time tsunami earthquake detection system, tsunami earthquake scenarios may be further developed by assuming a rigidity smaller than the currently used one of 40 GPa when calculating the slip amount from any

given moment magnitude. A dataset of earthquake events in different subduction zones suggest that the rigidity at the shallowest part of the subduction zone near the trench ranged from 5 to 40 GPa (Bilek & Lay, 1999). It has been shown that the use of smaller rigidity with a given moment magnitude, which equates to larger slip for tsunami earthquakes provides better tsunami impact predictions for these events (Tanioka et al., 2017). The development of tsunami earthquake scenarios may also need to consider the rupture velocity and kinematics as they could be important for the mechanism (Bell et al., 2014).

Normal faulting tsunamigenic earthquakes as the 5 December 2018 Mw 7.5 earthquake must be considered, especially in this region of the Vanuatu subduction zone as detailed by Roger et al (2021). Since 1995, four large normal faulting earthquakes had occurred in the Southern Vanuatu subduction zone in 1995 (Mw 7.7), 2004 (Mw 7.1), 2017 (Mw7.0), and 2018 (Mw 7.5) (Roger et al., 2021). Three of these four intraplate earthquakes in the outer-rise generated small to moderate tsunamis in the area (Roger et al., 2019; Sahal et al., 2010). Large tsunamigenic intraplate earthquakes with the potential to create disastrous tsunamis may also occur with normal faulting mechanisms, such as the 1933 Sanriku (Mw 8.4), 1977 Sumba (Mw 8.3), and 2017 Chiapas (Mw8.2) earthquakes (Gusman et al., 2009, 2018; Lynnes & Lay, 1988; Melgar et al., 2018; Tanioka & Sataka, 1996). There is currently no scenario in the database with normal faulting mechanism, thus an update that includes this earthquake mechanism is recommended.

As shown above, if the current pre-computed scenario were used to forecast the tsunami in the near field, the actual tsunami arrived after the predicted arrival time in New Caledonia, while the tsunami arrived before the predicted arrival time in Fiji. This is because the nearest pre-computed scenario is Westward the actual epicenter and the distance between scenarios is 150 km. Also, the plate boundary is curved around the earthquake source and the strike angles of fault model patches there varies from 260° to 300°. These suggest that the earthquake scenarios around the source region are not dense enough for those two countries. A simple rule for the distance between the scenarios based on the earthquake magnitude may be applied to expand the scenarios. The distance can be set to be at least half of the typical fault length for a given earthquake magnitude. This will give scenario distance of 50 km for earthquake scenarios with magnitudes from 7.5 to 7.9. Interpolation between scenarios may be more effective than having more scenarios and would be computationally more efficient to try to cover every possible earthquake that might occur. Although adding more scenarios is preferred for areas like the Southern Vanuatu subduction zone that have fault patches with a significant range (>20°) of strike angles.

Uniform slip models may be able to predict the tsunami fairly well as shown in this and other previous studies (e.g., An et al., 2018; Greenslade et al., 2011). However, the earthquake source complexity has an important role in uncertainty associated with near-field tsunami forecast, especially for great earthquakes with magnitudes larger than Mw 8.0 as indicated in previous studies (e.g., Davies & Griffin, 2020; Melgar et al., 2019; Mueller et al., 2021; Williamson et al., 2019). They found that homogenous slip models have frequently under estimated the peak tsunami amplitudes and the resulting tsunami hazard. New Zealand should consider updating its tsunami database to account for slip heterogeneity in earthquake scenarios with magnitudes larger than Mw 8.0. A very large number of non-uniform slip scenarios in the Hikurangi, Kermadec, and Puysegur subduction zones may be required for the case of New Zealand.

6.3. Rapid Response

In real-time, the response relied on threat-level maps derived from precalculated scenarios as described above. The NZTEP used modeling based on a coarse simplification of the earthquake source to validate the pre-calculated models. These simplified models used 50×100 km subduction zone unit sources and precalculated wave propagation Green's Functions from the propDB database accessed within the ComMIT software (Titov et al., 2011). One unit source (NV37b centered at 22.69°S–171.55°E) was used to represent the earthquake rupture with homogeneous slip. Based on a seismic magnitude of Mw7.7, initial response simulations calculated the tsunami wavefield resulting from 2 m slip. The resulting forecasts were used to augment the threat maps based on the pre-calculated scenarios described above. During the response, it was noted that forecast amplitudes were less than those recorded at coastal tide gauges and DARTs. To account for this discrepancy, a precautionary approach was taken and the modeled slip was adjusted to ~4 m, increasing the estimated earthquake magnitude to Mw7.9. This is compatible with the maximum slip amount of 4.1 m as described above. The pragmatic effect of this adjustment was to inform the expect duration of the Marine and Beach threat. We note that manual calibration

of the forecast is an interim step toward real-time inversion based forecasting. Current and future work is aimed at implementing inversion of DART data and improved forecasting. The Loyalty Islands earthquake and tsunami represent a valuable data point to help characterize the uncertainties involved in coarse discretization of the earthquake source and determine an acceptable trade-off between computational time and forecast accuracy.

7. Conclusions

We estimated the slip distribution of the 2021 Loyalty Islands earthquake from tsunami waveforms recorded at four DART stations and 24 coastal gauges. The slip model is assessed using simulations of seismic wave propagation and seismic data. The tsunami threat levels in coastal regions in New Zealand from the estimated slip distribution are then used as a reference map to evaluate the performance of our pre-computed earthquake scenario database selection and interpolation approaches for tsunami forecasting. The main results are:

1. The major slip region of the estimated fault slip distribution is located near the trench with maximum slip amount of 4.1 m. To evaluate the slip distribution estimated from the tsunami data, we compare observed and synthetic seismograms at 21 seismic stations. The seismic waves can be best reproduced by the estimated slip distribution with an assumed rupture velocity of 1.0 km/s.
2. The threat level of coastal regions in the West Coast of South Island of New Zealand is the same as some of those in the North Island even though the two locations are as far as 1000 km apart. The tsunami simulation results suggest that the tsunami was refracted by the Challenger Plateau and Bellona Basin which refocused some of its energy toward the West Coast of South Island.
3. A tsunami threat level map can be obtained by interpolating two nearest Mw 7.7 earthquake scenarios (WestMw7.7 and EastMw7.7) to the epicenter available in the database. In this case the tsunami waveforms recorded at the coastal gauges and DART stations show that the interpolated waveforms matched the observed tsunami amplitude and arrival time better than those from the two Mw 7.7 in the database. However, threat level validation or update from the analysis of tsunami data must be done with caution especially if the station azimuthal coverage is still poor during an event. The azimuthal coverage can increase as the tsunami propagates and is recorded by more stations.
4. The threat level maps from the nearest scenario and the interpolation both give accurate tsunami forecast for most warning zones in New Zealand. The uniform slip models can perform well relatively to the estimated slip, which show that rupture details are not critical for guiding tsunami warning in locations far away from the source of earthquakes with magnitudes up to Mw 7.7. A conservative forecast can be made by obtaining the higher threat level of the two maps.

Data Availability Statement

DART data are publicly available from New Zealand's GeoNet (https://tilde.geonet.org.nz/ui/data-exploration) (GNS Science, 2020). Tide gauge data available from Flanders Marine Institute (VLIZ); Intergovernmental Oceanographic Commission (IOC) (2021) (http://www.ioc-sealevelmonitoring.org/). Seismic wave simulations and tsunami threat level database creation were performed using the New Zealand eScience Infrastructure (NeSI) high-performance computing system (https://www.nesi.org.nz). Figures in the main text were made using GMT (https://www.generic-mapping-tools.org) (Wessel & Smith, 1998) (Figures 1–4 and 8 and 9) and MATLAB (www.mathworks.com) (Figures 5, 10 and 11) softwares. GEBCO gridded bathymetric data can be downloaded from (https://www.gebco.net/data_and_products/gridded_bathymetry_data/).

References

Akaike, H. (1980). Seasonal adjustment by a Bayesian modeling. *Journal of Time Series Analysis*, *1*(1), 1–13. https://doi.org/10.1111/j.1467-9892.1980.tb00296.x

An, C., Liu, H., Ren, Z., & Yuan, Y. (2018). Prediction of tsunami waves by uniform slip models. *Journal of Geophysical Research: Oceans*, *123*(11), 8366–8382. https://doi.org/10.1029/2018jc014363

Bassin, C., Laske, G., & Masters, G. (2000). The current limits of resolution for surface wave tomography in North America. *EOS Transactions American Geophysical Union*, *81*(48), F897.

Bell, R., Holden, C., Power, W., Wang, X., & Downes, G. (2014). Hikurangi margin tsunami earthquake generated by slow seismic rupture over a subducted seamount. *Earth and Planetary Science Letters*, *397*, 1–9. https://doi.org/10.1016/j.epsl.2014.04.005

Bilek, S. L., & Lay, T. (1999). Rigidity variations with depth along interplate megathrust faults in subduction zones. *Nature*, *400*(6743), 443–446. https://doi.org/10.1038/22739

Blaser, L., Krüger, F., Ohrnberger, M., & Scherbaum, F. (2010). Scaling relations of earthquake source parameter estimates with special focus on subduction environment. *Bulletin of the Seismological Society of America*, *100*(6), 2914–2926. https://doi.org/10.1785/0120100111

Burbidge, D. R., & Roger, J. H. (2022). New Zealand DART buoys network effectiveness report for the period between 18 May 2020 and 31 December 2021. GNS Science consultancy report 2022/16LR (p. 12).

Calmant, S., Pelletier, B., Bevis, M., Taylor, F., Lebellegard, P., & Phillips, D. (2003). New insights on the tectonics of the New Hebrides subduction zone based on GPS results. *Journal of Geophysical Research*, *108*(B6), 2319–2340. https://doi.org/10.1029/2001jb000644

Davies, G., & Griffin, J. (2020). Sensitivity of probabilistic tsunami hazard assessment to far-field earthquake slip complexity and rigidity depth-dependence: Case study of Australia. *Pure and Applied Geophysics*, *177*(3), 1521–1548. https://doi.org/10.1007/s00024-019-02299-w

Duphil, M., Aucan, J., Lefèvre, J., Pelletier, B., Roger, J., & Thomas, B. (2021). Tsunami hazard assessment in New Caledonia. *TsuInfo Alert*, *23*(1). https://www.dnr.wa.gov/publications/ger_tsuinfo_2021_v23_no1.pdf

Ekström, G., Nettles, M., & Dziewoński, A. M. (2012). The global CMT project 2004–2010: Centroid-moment tensors for 13,017 earthquakes. *Physics of the Earth and Planetary Interiors*, *200*, 1–9.

Flanders Marine Institute (VLIZ); Intergovernmental Oceanographic Commission (IOC). (2021). Sea level station monitoring facility. *Dataset*. https://doi.org/10.14284/482

Fry, B., Gledhill, K. R., & Benites, R. A. (2018). Ground motions in New Zealand from Kermadec megathrust earthquakes. Lower Hutt, N.Z: GNS Science. *GNS Science report 2018/33*. 17. https://doi.org/10.21420/7J43-G338

Fry, B., McCurrach, S.-J., Gledhill, K. R., Power, W. L., Williams, M., Angove, M., et al. (2020). Sensor network warns of stealth tsunamis. *Eos*, *101*. https://doi.org/10.1029/2020EO144274

Fujii, Y., & Satake, K. (2008). Tsunami sources of the November 2006 and January 2007 great Kuril earthquakes. *Bulletin of the Seismological Society of America*, *98*(3), 1559–1571. https://doi.org/10.1785/0120070221

Furuyama, S., & Maihara, Y. (2014). High resolution & high performance tsunami run-up simulation. *Journal of Ecotechnology Research*, *17*(2), 79–83.

Gica, E. (2008). Development of the forecast propagation database for NOAA's Short-term inundation forecast for tsunamis (SIFT).

GNS Science. (2020). NZ deep-ocean assessment and reporting of tsunami (DART) data set . *GNS Science*. https://doi.org/10.21420/8TCZ-TV02

Greenslade, D., Allen, S. C. R., & Simanjuntak, M. A. (2011). An evaluation of tsunami forecasts from the T2 scenario database. *Pure and Applied Geophysics*, *168*, 1137–1151. https://doi.org/10.1007/s00024-010-0229-3

Gusman, A. R., Murotani, S., Satake, K., Heidarzadeh, M., Gunawan, E., Watada, S., & Schurr, B. (2015). Fault slip distribution of the 2014 Iquique, Chile, earthquake estimated from ocean-wide tsunami waveforms and GPS data. *Geophysical Research Letters*, *42*(4), 1053–1060. https://doi.org/10.1002/2014gl062604

Gusman, A. R., Kaneko, Y., Power, W., & Burbidge, D. (2020). Source process for two enigmatic repeating vertical-T CLVD tsunami earthquakes in the Kermadec Ridge. *Geophysical Research Letters*, *47*. https://doi.org/10.1029/2020GL087805

Gusman, A. R., Lukovic, B., & Peng, B. (2020). Tsunami threat level database update: Regional sources and tsunami warning text. *Lower Hutt, N.Z: GNS Science. GNS Science report 2019/83. 57 p.* https://doi.org/10.21420/PTDC-NS18

Gusman, A. R., Mulia, I. E., & Satake, K. (2018). Optimum sea surface displacement and fault slip distribution of the 2017 Tehuantepec earthquake (Mw 8.2) in Mexico estimated from tsunami waveforms. *Geophysical Research Letters*, *45*(2), 646–653. https://doi.org/10.1002/2017gl076070

Gusman, A. R., Tanioka, Y., Kobayashi, T., Latief, H., & Pandoe, W. (2010). Slip distribution of the 2007 Bengkulu earthquake inferred from tsunami waveforms and InSAR data. *Journal of Geophysical Research*, *115*(B12). https://doi.org/10.1029/2010jb007565

Gusman, A. R., Tanioka, Y., MacInnes, B. T., & Tsushima, H. (2014). A methodology for near-field tsunami inundation forecasting: Application to the 2011 Tohoku tsunami. *Journal of Geophysical Research: Solid Earth*, *119*(11), 8186–8206. https://doi.org/10.1002/2014jb010958

Gusman, A. R., Tanioka, Y., Matsumoto, H., & Iwasaki, S. I. (2009). Analysis of the tsunami generated by the great 1977 Sumba earthquake that occurred in Indonesia analysis of the tsunami generated by the great 1977 Sumba earthquake that occurred in Indonesia. *Bulletin of the Seismological Society of America*, *99*(4), 2169–2179. https://doi.org/10.1785/0120080324

Harig, S., Immerz, A., WenizaGriffin, J., Weber, B., Babeyko, A., rakowsky, N., et al. (2019). The tsunami scenario database of the Indonesia tsunami early warning system (InaTEWS): Evolution of the coverage and the involved modeling approaches. *Pure and Applied Geophysics*, *177*, 1379–1401. https://doi.org/10.1007/s00024-019-02305-1

Hayes, G. P., Moore, G. L., Portner, D. E., Hearne, M., Flamme, H., Furtney, M., & Smoczyk, G. M. (2018). Slab2, a comprehensive subduction zone geometry model. *Science*, *362*(6410), 58–61. https://doi.org/10.1126/science.aat4723

Heidarzadeh, M., & Gusman, A. R. (2021). Source modeling and spectral analysis of the Crete tsunami of 2nd may 2020 along the Hellenic subduction zone, offshore Greece. *Earth Planets and Space*, *73*(1), 1–16. https://doi.org/10.1186/s40623-021-01394-4

Heidarzadeh, M., Satake, K., Murotani, S., Gusman, A. R., & Watada, S. (2015). Deep-water characteristics of the trans-Pacific tsunami from the 1 April 2014 M w 8.2 Iquique, Chile earthquake. *Pure and Applied Geophysics*, *172*(3), 719–730. https://doi.org/10.1007/s00024-014-0983-8

Hjörleifsdóttir, V., Kanamori, H., & Tromp, J. (2009). Modeling 3-D wave propagation and finite slip for the 1998 Balleny Islands earthquake. *Journal of Geophysical Research*, *114*(B3).

Ho, T. C., Satake, K., Watada, S., & Fujii, Y. (2019). Source estimate for the 1960 Chile earthquake from joint inversion of geodetic and transoceanic tsunami data. *Journal of Geophysical Research: Solid Earth*, *124*(3), 2812–2828. https://doi.org/10.1029/2018jb016996

Holden, C., Kaneko, Y., D'Anastasio, E., Benites, R., Fry, B., & Hamling, I. J. (2017). The 2016 Kaikōura earthquake revealed by kinematic source inversion and seismic wavefield simulations: Slow rupture propagation on a geometrically complex crustal fault network. *Geophysical Research Letters*, *44*(22), 11–320. https://doi.org/10.1002/2017gl075301

Hoshiba, M., & Ozaki, T. (2014). Earthquake early warning and tsunami warning of the Japan Meteorological Agency, and their performance in the 2011 off the Pacific coast of Tohoku earthquake Mw 9.0). In *Early warning for geological disasters* (pp. 1–28). Springer. https://doi.org/10.1007/978-3-642-12233-0_1

Ioualalen, M., Pelletier, B., & Gordillo, G. S. (2017). Investigating the March 28th 1875 and the September 20th 1920 earthquakes/tsunamis of the southern Vanuatu arc, offshore loyalty islands, New Caledonia. *Tectonophysics*, *709*, 20–38. https://doi.org/10.1016/j.tecto.2017.05.006

Kanamori, H. (1972). Mechanism of tsunami earthquakes. *Physics of the Earth and Planetary Interiors*, *6*(5), 346–359. https://doi.org/10.1016/0031-9201(72)90058-1

Kanamori, H., & Rivera, L. (2008). Source inversion of Wphase: Speeding up seismic tsunami warning. *Geophysical Journal International*, *175*(1), 222–238. https://doi.org/10.1111/j.1365-246x.2008.03887.x

Komatitsch, D., & Tromp, J. (2002a). Spectral-element simulations of global seismic wave propagation—I. Validation. *Geophysical Journal International*, *149*(2), 390–412. https://doi.org/10.1046/j.1365-246x.2002.01653.x

Komatitsch, D., & Tromp, J. (2002b). Spectral-element simulations of global seismic wave propagation—II. Three-dimensional models, oceans, rotation and self-gravitation. *Geophysical Journal International*, *150*(1), 303–318. https://doi.org/10.1046/j.1365-246x.2002.01716.x

Lawson, C. L., & Hanson, R. J. (1995). *Solving least squares problems*. Society for Industrial and Applied Mathematics.

Liu, P. L. F., Woo, S. B., & Cho, Y. S. (1998). *Computer programs for tsunami propagation and inundation*. Cornell University. Technical Report.

Lorito, S., Piatanesi, A., Cannelli, V., Romano, F., & Melini, D. (2010). Kinematics and source zone properties of the 2004 Sumatra-Andaman earthquake and tsunami: Nonlinear joint inversion of tide gauge, satellite altimetry, and GPS data. *Journal of Geophysical Research*, *115*(B2). https://doi.org/10.1029/2008jb005974

Lynnes, C. S., & Lay, T. (1988). Source process of the great 1977 Sumba earthquake. *Journal of Geophysical Research*, *93*(B11), 13407–13420. https://doi.org/10.1029/jb093ib11p13407

Matias, L., Baptista, M. A., Omira, R., Annunziato, A., Franchello, G., & Carrilho, F. (2012). Third generation tsunami scenario matrix for the Portuguese tsunami early warning system. *Proceedings of the 15 WCEE, Lisboa, Portugal*. https://core.ac.uk/download/pdf/38626266.pdf

Melgar, D., Ruiz-Angulo, A., Garcia, E. S., Manea, M., Manea, V. C., Xu, X., et al. (2018). Deep embrittlement and complete rupture of the lithosphere during the M w 8.2 Tehuantepec earthquake. *Nature Geoscience*, *11*(12), 955–960. https://doi.org/10.1038/s41561-018-0229-y

Melgar, D., Williamson, A., & Salazar-Monroy, E. (2019). Differences between heterogenous and homogenous slip in regional tsunami hazards modelling. *Geophysical Journal International*, *219*, 553–562.

Mueller, C., Burbidge, D., & Power, W. (2021). Regional tsunami forecasting: Uncertainties due to non-uniform slip. *Pure and Applied Geophysics*, *178*(12), 5155–5173. https://doi.org/10.1007/s00024-021-02845-5

Mulia, I. E., Gusman, A. R., & Satake, K. (2018). Alternative to non-linear model for simulating tsunami inundation in real-time. *Geophysical Journal International*, *214*(3), 2002–2013. https://doi.org/10.1093/gji/ggy238

Mulia, I. E., Gusman, A. R., & Satake, K. (2020). Applying a deep learning algorithm to tsunami inundation database of megathrust earthquakes. *Journal of Geophysical Research: Solid Earth*, *125*(9), e2020JB019690. https://doi.org/10.1029/2020jb019690

Nagasu, K., Sano, K., Kono, F., & Nakasato, N. (2017). FPGA-based tsunami simulation: Performance comparison with GPUs, and roofline model for scalability analysis. *Journal of Parallel and Distributed Computing*, *106*, 153–169. https://doi.org/10.1016/j.jpdc.2016.12.015

National Emergency Management Agency [Nema]. (2020). *Tsunami advisory and warning plan: Supporting plan [SP 01/20]*. National Emergency Management Agency. Retrieved from https://www.civildefence.govt.nz/assets/Uploads/publications-/Supporting-Plans/Tsunami-Advisory-and-Warning-Plan-Supporting-Plan-Update-Jun-2020.pdf

Neil, H., Orpin, A., Nodder, S., Mitchell, J., Northcote, L., Mackay, K., & Kane, T. (2015). Large canyon-channel complexes from South Island of New Zealand show contrasting morphologies. *AAPG Asia Pacific Region, Geoscience Technology Workshop, Modern Depositional Systems as Analogues for Petroleum Reservoirs, April 21-22, 2015, Wellington, New Zealand*. https://www.searchanddiscovery.com/abstracts/pdf/2015/90235gtw/abstracts/ndx_neil.pdf

Newman, A. V., Hayes, G., Wei, Y., & Convers, J. (2011). The 25 October 2010 Mentawai tsunami earthquake, from real-time discriminants, finite-fault rupture, and tsunami excitation. *Geophysical Research Letters*, *38*(5). https://doi.org/10.1029/2010gl046498

Okada, Y. (1985). Surface deformation due to shear and tensile faults in a half-space. *Bulletin of the Seismological Society of America*, *75*(4), 1135–1154. https://doi.org/10.1785/bssa0750041135

Okal, E. A. (1988). Seismic parameters controlling far-field tsunami amplitudes: A review. *Natural Hazards*, *1*(1), 67–96. https://doi.org/10.1007/bf00168222

Onat, Y., & Yalciner, A. C. (2013). Initial stage of database development for tsunami warning system along Turkish coasts. *Ocean Engineering*, *74*, 141–154. https://doi.org/10.1016/j.oceaneng.2013.09.008

Power, W., Wallace, L., Wang, X., & Reyners, M. (2012). Tsunami hazard posed to New Zealand by the Kermadec and southern new Hebrides subduction margins: An assessment based on plate boundary kinematics, interseismic coupling, and historical seismicity. *Pure and Applied Geophysics*, *169*(1), 1–36. https://doi.org/10.1007/s00024-011-0299-x

Power, W. L. (2017). A tool for rapid tsunami threat (RTTM) generation. Lower Hutt, N.Z: GNS Science. *GNS Science report 2017/37*, 30. https://doi.org/10.21420/G2463J

Power, W. L., Fry, B., Gusman, A. R., Burbidge, D. R., Brewer, M., & Wang, X. (2018). DART buoys network design. *GNS Science Consultancy Report*, 53. https://doi.org/10.2018/147

Reymond, D., Okal, E. A., Hébert, H., & Bourdet, M. (2012). Rapid forecast of tsunami wave heights from a database of pre-computed simulations, and application during the 2011 Tohoku tsunami in French Polynesia. *Geophysical Research Letters*, *39*(11), a–n. https://doi.org/10.1029/2012GL051640

Riquelme, S., & Fuentes, M. (2021). Tsunami efficiency due to very slow earthquakes. *Seismological Research Letters*, *92*, 2998–3006. https://doi.org/10.1785/0220200198

Ritsema, J., Deuss, A., Van Heijst, H. J., & Woodhouse, J. H. (2011). S40RTS: A degree-40 shear-velocity model for the mantle from new Rayleigh wave dispersion, teleseismic traveltime and normal-mode splitting function measurements. *Geophysical Journal International*, *184*(3), 1223–1236. https://doi.org/10.1111/j.1365-246x.2010.04884.x

Roger, J., Pelletier, B., & Aucan, J. (2019). Update of the tsunami catalogue of New Caledonia using a decision table based on seismic data and marigraphic records. *Natural Hazards and Earth System Sciences*, *19*, 1471–1483. https://doi.org/10.5194/nhess-19-1471-2019

Roger, J., Pelletier, B., Duphil, M., Lefèvre, J., Aucan, J., Lebellegard, P., et al. (2021). The Mw 7.5 Tadine (Maré, loyalty is.) earthquake and related tsunami of December 5, 2018: Implications for tsunami hazard assessment in New Caledonia. Natural hazards and Earth system Sciences. *Discussions*. https://doi.org/10.5194/nhess-2021-58

Romano, F., Piatanesi, A., Lorito, S., Tolomei, C., Atzori, S., & Murphy, S. (2016). Optimal time alignment of tide-gauge tsunami waveforms in nonlinear inversions: Application to the 2015 Illapel (Chile) earthquake. *Geophysical Research Letters*, *43*(21), 11–226. https://doi.org/10.1002/2016gl071310

Rowden, A. A., Clark, M. R., & Wright, I. C. (2005). Physical characterisation and a biologically focused classification of "seamounts" in the New Zealand region. *New Zealand Journal of Marine & Freshwater Research*, *39*, 1039–1059. https://doi.org/10.1080/00288330.2005.9517374

Sahal, A., Pelletier, B., Chatelier, J., Lavigne, F., & Schindelé, F. (2010). A catalog of tsunamis in New Caledonia from 28 March 1875 to 30 September 2009. *Comptes Rendus Geoscience*, *342*, 437–444. https://doi.org/10.1016/j.crte.2010.01.013

Satake, K. (1995). Linear and nonlinear computations of the 1992 Nicaragua earthquake tsunami. *Pure and Applied Geophysics*, *144*(3), 455–470. https://doi.org/10.1007/978-3-0348-7279-9_6

Satake, K., Nishimura, Y., Putra, P. S., Gusman, A. R., Sunendar, H., Fujii, Y., et al. (2013). Tsunami source of the 2010 Mentawai, Indonesia earthquake inferred from tsunami field survey and waveform modeling. *Pure and Applied Geophysics*, *170*(9), 1567–1582. https://doi.org/10.1007/s00024-012-0536-y

Shepard, D. (1968). A two-dimensional interpolation function for irregularly-spaced data. In *Proceedings of the 1968 23rd ACM national conference* (pp. 517–524). https://doi.org/10.1145/800186.810616

Tanioka, Y., Miranda, G. J. A., Gusman, A. R., & Fujii, Y. (2017). Method to determine appropriate source models of large earthquakes including tsunami earthquakes for tsunami early warning in Central America. *Pure and Applied Geophysics*, *174*(8), 3237–3248. https://doi.org/10.1007/s00024-017-1630-y

Tanioka, Y., & Sataka, K. (1996). Fault parameters of the 1896 Sanriku tsunami earthquake estimated from tsunami numerical modeling. *Geophysical Research Letters*, *23*(13), 1549–1552. https://doi.org/10.1029/96gl01479

Tatehata, H. (1997). The new tsunami warning system of the Japan Meteorological Agency. In *Perspectives on tsunami hazard reduction* (pp. 175–188). Springer. https://doi.org/10.1007/978-94-015-8859-1_12

Titov, V. V., Moore, C. W., Greenslade, D. J. M., Pattiaratchi, C., Badal, R., Synolakis, C. E., & Kânoğlu, U. (2011). A new tool for inundation modeling: Community modeling interface for tsunamis (ComMIT). *Pure and Applied Geophysics*, *168*, 2121–2131. https://doi.org/10.1007/s00024-011-0292-4

Uruski, C. I. (2010). New Zealand's deepwater Frontier. *Marine and Petroleum Geology*, *27*(9), 2005–2026. https://doi.org/10.1016/j.marpetgeo.2010.05.010

USGS. (2021). Retrieved from https://earthquake.usgs.gov/earthquakes/eventpage/us6000dg77/executive

Wang, X., & Liu, P. L. F. (2006). An analysis of 2004 Sumatra earthquake fault plane mechanisms and Indian Ocean tsunami. *Journal of Hydraulic Research*, *44*(2), 147–154. https://doi.org/10.1080/00221686.2006.9521671

Wang, X., & Power, W. L. (2011). Comcot: A tsunami generation, propagation and run-up model. *Lower Hutt (NZ): GNS Science (GNS Science report; 2011/43)*, 121.

Wang, Y., Maeda, T., Satake, K., Heidarzadeh, M., Su, H., Sheehan, A. F., & Gusman, A. R. (2019). Tsunami data assimilation without a dense observation network. *Geophysical Research Letters*, *46*(4), 2045–2053. https://doi.org/10.1029/2018gl080930

Watada, S., Kusumoto, S., & Satake, K. (2014). Traveltime delay and initial phase reversal of distant tsunamis coupled with the self-gravitating elastic Earth. *Journal of Geophysical Research: Solid Earth*, *119*(5), 4287–4310. https://doi.org/10.1002/2013jb010841

Wessel, P., & Smith, W. H. (1998). New, improved version of generic mapping tools released [Software]. *Eos, Transactions American Geophysical Union*, *79*(47), 579. https://doi.org/10.1029/98eo00426

Williamson, A., Melgar, D., & Rim, D. (2019). The effect of earthquake kinematics on tsunami propagation. *Journal of Geophysical Research: Solid Earth*, *124*, 11639–11650. https://doi.org/10.1029/2019jb017522

Yabuki, T., & Matsu'Ura, M. (1992). Geodetic data inversion using a Bayesian information criterion for spatial distribution of fault slip. *Geophysical Journal International*, *109*(2), 363–375. https://doi.org/10.1111/j.1365-246x.1992.tb00102.x